2 Light scattering by irregularly shaped particles with sizes comparable to the wavelength

Evgenij S. Zubko

2.1 Introduction

Light scattering by single irregularly shaped particles whose sizes are comparable with wavelength plays an important role in numerous remote-sensing applications. It especially concerns applications dealing with both terrestrial and cosmic dust particles having truly irregular and random structure. The knowledge of the scattering by single irregular particles is absolutely necessary for a realistic modeling and successful interpretation of measurements of light scattering by a powder-like surface, such as, soils, sand-drift or planetary regolith. Note that, though the multiple scattering between constituent particles could significantly dominate over single scattering, it is quite evident that the one is a function of other.

The study light scattering by cosmic dust particles is a difficult problem, in particular, because there is an obvious lack of information on the structure of such particles. Indeed, unlike terrestrial dust, a sampling of cosmic dust within the Solar system is an extremely delicate and expensive undertaking; whereas, the sampling of dust particles beyond the Solar system is practically impossible. So far, there is only one successful attempt at such sampling, namely, the *Stardust* mission to comet 81P/Wild 2 (see, e.g., Brownlee *et al.*, 2006). This space probe collected dust particles in the environment of a cometary nucleus (the closest distance was 236 km) onto extremely porous silica foam, called aerogel. Though the density of aerogel varies in the range 0.01–0.05 g/cm^3, this substance is quite tenacious. For instance, a piece of aerogel weighing only 2 grams can support a brick having a weight of 2.5 kg (see picture in http://stardust.jpl.nasa.gov/photo/aerogel.html). When capturing dust particles, *Stardust* approached comet 81P/Wild 2 at a relative velocity of 6 km/s. Therefore, cometary particles experienced a highly energetic collision with the aerogel collector. Interestingly, the typical length of tracks of dust particles captured in aerogel is about one centimeter (Burnett, 2006), which implies a very fast deceleration of particles. As a consequence, micron-sized dust particles did not preserve their original structure; they were broken down into many small compact constituents and heated above ∼2000 K (Brownlee *et al.*, 2006).

A significantly less-destructive method to sample cosmic dust particles is to collect them in the Earth stratosphere using high-altitude airplanes (e.g., Brownlee *et al.*, 1995; Jessberger *et al.*, 2001; Busemann *et al.*, 2009). For example, Fig. 2.1

A.A. Kokhanovsky (ed.), *Light Scattering Reviews 6: Light Scattering and Remote Sensing of Atmosphere and Surface*, Springer Praxis Books, DOI 10.1007/978-3-642-15531-4_2,

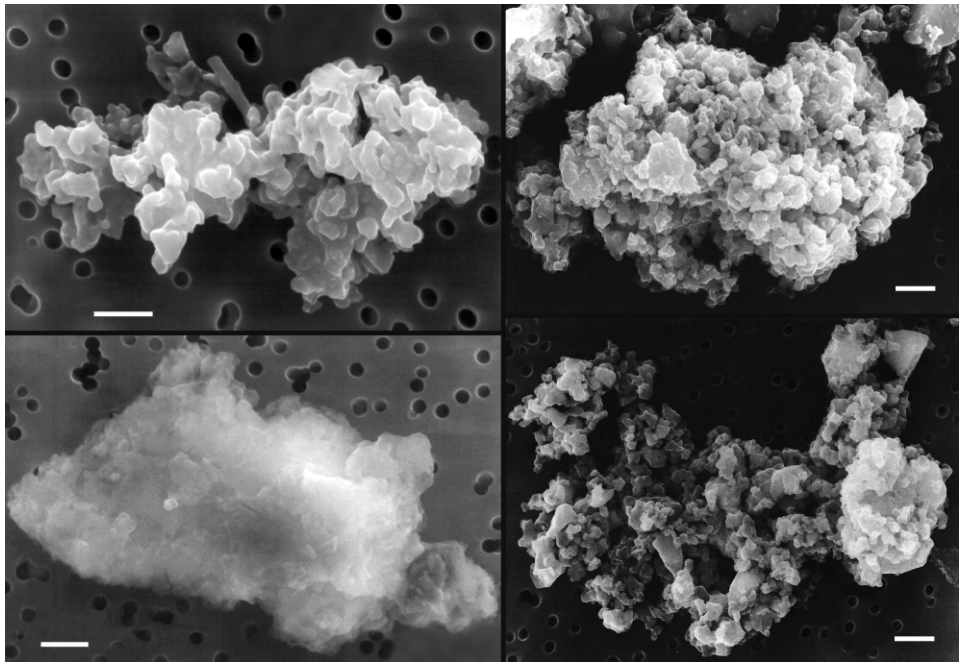

Fig. 2.1. Images of four interplanetary dust particles (IDPs) collected in the stratosphere, having probable cometary origin (adapted from Dai and Bradley, 2001; Hanner and Bradley, 2001; Jessberger *et al.*, 2001). The white line in each panel corresponds to 1 μm size.

presents images of four interplanetary dust particles (IDPs) collected in this way (adapted from Dai and Bradley, 2001; Jessberger *et al.*, 2001; Hanner and Bradley, 2004) and probably having a cometary origin. In general, IDPs originated either from asteroids or comets (e.g., Brownlee *et al.*, 1995). Though IDPs enter the atmosphere at velocities typically higher than 12 km/s, the air does not affect their structure as strongly as aerogel. Therefore, micron-sized particles may preserve their original structure. Indeed, as one can see in Fig. 2.1, IDPs with fluffy structure can be captured in the stratosphere. On the other hand, the specific parent bodies of IDPs captured in the stratosphere are not as well known as in the case of sampling directly near a comet or asteroid and, thus, additional efforts are required to determine the origin of collected particles (Brownlee *et al.*, 1995). Nevertheless, when sampling dust particles shortly after Earth passes through the dust tail of some comet, the origin of the collected particles can be established with some confidence. Using such a dedicated sampling method in the stratosphere, there were successful campaigns to catch dust particles from comet 26P/Grigg–Skjellerup (Busemann *et al.*, 2009). Fig. 2.2 reproduces images of some samples obtained by Busemann *et al.* (2009).

As one can see in Figs. 2.1 and 2.2, all IDPs are quite irregular in appearance. On the other hand, there is also a dramatic difference between particles; evidently, they do not belong to one morphologic type. Particles shown in Figs. 2.1 and 2.2 could be classified into, at least, two distinctive groups, namely, relatively compact

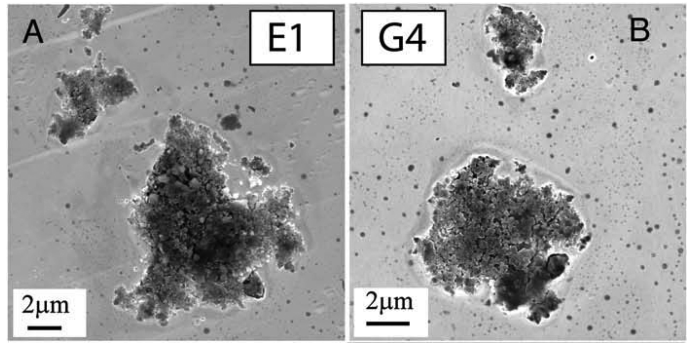

Fig. 2.2. Images of dust particles originating from comet 26P/Grigg-Skjellerup (adapted from Busemann *et al.*, 2009).

and fluffy. However, the difference in morphology of dust particles has an influence on their light scattering and understanding that interrelationship is necessary for the successful development of remote-sensing techniques.

The primary goal of this review is to show how different parameters of light scattering, such as angular profiles of intensity and degree of linear polarization, geometric and single-scattering albedo, asymmetry parameter, cross-sections of extinction and absorption, vary for different types of irregularly shaped particles. Note that, due to random variations in the structure of different samples belonging to one morphologic type, their light-scattering properties can vary dramatically. Therefore, in order to discriminate the impact of a particular characteristic morphology type from that caused by peculiarities of a given sample particle, it is necessary to perform a statistically reliable averaging of light-scattering properties over many samples for each type of particles.

Using the discrete dipole approximation (DDA), we simulate light scattering by six substantially different types of irregularly shaped particles. In most of cases, light-scattering properties of each type of irregular particles have been averaged over a few hundreds of samples. Simultaneously, each type of irregularly shaped particle is studied at three different refractive indices m, representing the abundant species of cosmic dust, such as, water ice, magnesium-rich silicates, and organic refractory in the visible band. Note that these refractive indices also can be associated with some terrestrial aerosols. Furthermore, each case of m is considered over a wide range of particle sizes comparable with wavelength λ of the incident radiation. The large generated data set allows us to make a systematic comparison of light-scattering properties of irregularly shaped particles with different morphology.

2.2 Modeling light scattering by irregularly shaped particles

2.2.1 Models of irregularly shaped particles

We study six types of irregularly shaped particles that could be labeled as follows: agglomerated debris particles, pocked spheres, rough-surface spheres, strongly damaged spheres, debris of spheres, and Gaussian random particles. Example images

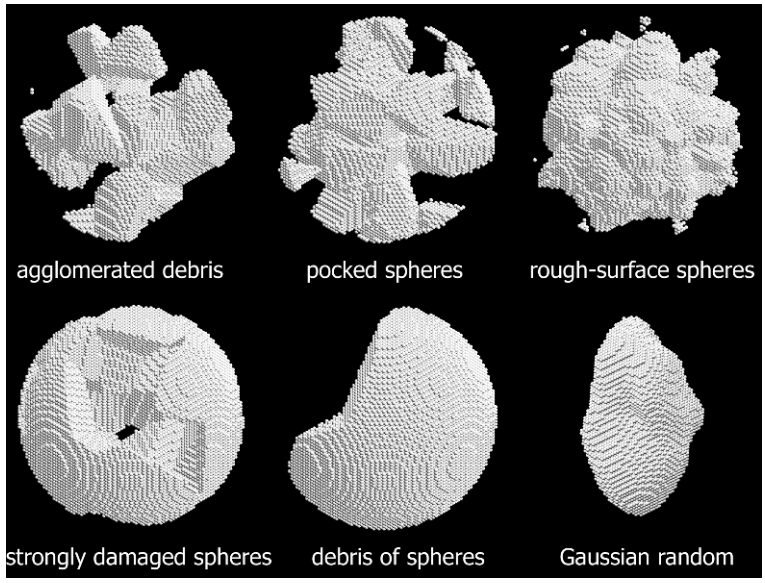

Fig. 2.3. Samples of irregularly shaped particles of six different types.

of these particles are shown in Fig. 2.3. One can see that all particles appear to be essentially non-spherical and reveal a wide variety of particle structures. Indeed, there are highly compact structures, such as rough-surface spheres and Gaussian random particles. Fluffy structure is represented in agglomerated debris particles and pocked spheres, while heavily damaged spheres and debris of spheres correspond to moderate cases.

Except for the Gaussian random particles, irregularly shaped particles have been generated using one algorithm, which is as follows. In computer memory, a spherical volume is filled with a regular cubic lattice that is considered as the initial matrix of the irregular particles. We consider the initial matrix consisting of 137,376 cells. In the process, the elements of the cubic lattice inside the initial matrix are assigned material properties corresponding to the refractive indices of the particles. All cubic cells forming this initial matrix are divided into two groups: cells belonging to the surface layer and cells internal to the surface layer. The depth of the surface layer is a parameter of our model. For instance, in the case of agglomerated debris particles and rough-surface spheres, the depth takes a value of only 0.5% of the radius of the initial matrix; i.e., the surface layer is formed only by dipoles having direct contact with the surrounding empty space. In the case of pocked spheres, the depth is 12.5% of the radius of the initial matrix. Strongly damaged spheres and debris of spheres are generated having no surface layer; i.e., all cells of the initial matrix are treated as internal.

Once cells forming the initial matrix are divided into two sub-groups, we choose seed cells for empty space and material at random. In general, we distinguish two types of seed cells for empty space: those belonging to the surface layer and those belonging to the internal volume; whereas, seed cells for the material are allocated only among internal cells. For instance, agglomerated debris particles are generated

with 100 seed cells of empty space randomly chosen in the surface layer, 20 seed cells of empty space, and 21 seed cells of material randomly allocated throughout the internal volume. For rough-surface spheres, the numbers of seed cells are 1,200 for empty space in the surface layer, 150 for material and 0 for empty space within the interior. In the case of pocked spheres they are 100, 50, and 0, respectively. Because heavily damaged spheres and debris of spheres are generated with zero depth of the surface layer, it implies that the number of seed cells for empty space allocated in the surface layer is 0. For strongly damaged spheres, there are 20 seed cells of empty space and 21 seed cells of material; whereas, for debris of spheres the numbers of seed cells of empty space and material are both equal to 4. The final stage of generating a target particle is to evaluate the rest of the cells forming the initial matrix: step-by-step, each cell distinct from the seed cells is assigned with the same optical properties as that of the nearest seed cell. Agglomerated debris particles, pocked spheres, rough-surface spheres, and heavily damaged spheres have been previously studied in Zubko *et al.* (2006; 2009a); in these papers, further images of particles can be also found.

Using the algorithm described in Muinonen *et al.* (1996), we have generated a set of 100 samples of random Gaussian particles. This type of particle is parameterized by the relative radius standard deviation σ and power law index in the covariance function of the logarithmic radius ν, which take values of 0.245 and 4, respectively. Unlike other types of irregular particles involved in this study, random Gaussian particles have a quite smooth surface; nevertheless, their shape is significantly non-spherical. Note that light scattering by exactly the same ensemble of shapes of random Gaussian particles have been studied in Zubko *et al.* (2007), and additional images of sample particles can be found therein.

Two important parameters characterizing irregularly shaped particles are the radius of the circumscribing sphere r_{cs} and the packing density ρ of particle material. Note that these parameters do not describe completely the properties of a particle. The more complicated the structure, the more parameters are needed to describe it. Nevertheless, even considering the effects of varying these two parameters may significantly improve our understanding of scattering peculiarities of irregularly shaped particles. In cases of non-Gaussian irregular particles, the radius of the circumscribing sphere is close to the radius of the initial matrix; the difference does not exceed 1%. We approximate the circumscribing sphere with the largest sample from the set of 100 particles to preserve the size distribution of random Gaussian particles obtained with original algorithm described by Muinonen *et al.* (1996). We define the packing density ρ of a particle as the ratio of volume occupied by the particle material to volume of the circumscribing sphere. We would like to stress that, in the general case, different sample particles of given morphology do not have the same volume of material, so ρ varies randomly from one sample to another. Fig. 2.4 shows the probability distribution of packing density ρ for all six types of irregular particles. Here, curve (1) corresponds to agglomerated debris particles, (2) to pocked spheres, (3) to rough-surface spheres, (4) to heavily damaged spheres, (5) to debris of spheres, and (6) to random Gaussian particles. As one can see, the compact morphologies, such as rough-surface spheres and random Gaussian particles reveal quite narrow distributions of ρ. Pocked spheres also demonstrate a rather narrow distribution of ρ, though not as much as particles

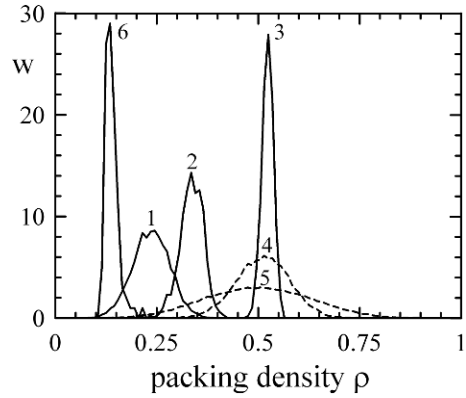

Fig. 2.4. Probability distribution of packing density ρ for six types of irregularly shaped particles.

with compact structure. Simultaneously, agglomerated debris particles have a significantly relaxed distribution of packing density, which, to some extent, is similar to that of heavily damaged spheres. Finally, debris of spheres reveal a quite wide distribution of ρ. Note that three types of irregular particles, namely, rough-surface spheres, heavily damaged spheres, and debris of spheres have almost the same average values of packing density $\langle\rho\rangle$: 0.523, 0.512, and 0.500, respectively. In the case of pocked spheres, $\langle\rho\rangle$ is 0.336; whereas, the average packing density of agglomerated debris particles is 0.236. Note that, according to our definition of packing density, its average is an anomalously low value of 0.139 in the case of random Gaussian particles. However, as one can see in Fig. 2.3, these particles are quite compact in appearance. Obviously, such an underestimation of the average packing density results from the elongated shape of the Gaussian particles. Therefore, in what follows, we refer random Gaussian particles as those having quite compact structure. Since non-Gaussian irregular particles are more or less equally elongated in all directions, in these cases, our definition provides accurate estimations of the average packing density.

2.2.2 The DDA method and parameters

We use the DDA to perform our light-scattering calculations (e.g., Draine, 1988; Draine and Flatau, 1994; Yurkin and Hoekstra, 2007; Zubko *et al.*, 2010). This approach allows us to consider particles with arbitrary shape and internal composition. In the DDA, a target particle is modeled with an array of small constituent volumes that together reproduce the shape and internal optical properties of the original particles. These constituent volumes must be significantly smaller than the wavelength of the incident electromagnetic wave, and their scattering properties take the form of a simple analytic expression (i.e., Rayleigh approximation). Due to such a replacement, one can reduce the light-scattering problem to a system of linear algebraic equations. One optional restriction on constituent volumes is that they be located in a regular cubic lattice to allow use of the fast Fourier transformation (FFT) and, thus, dramatically accelerate computations (Goodman

et al., 1991). We use our well-tested implementation of the DDA to perform the calculations of this manuscript (Zubko *et al.*, 2003, 2010; Penttilä *et al.*, 2007).

An important parameter specifying the DDA applicability is the size of the cubic lattice d. In application to irregular particles, the DDA provides accurate numerical result under the condition $kd|m| \leq 1$, where wavenumber $k = 2\pi/\lambda$, λ is the wavelength of the incident electromagnetic wave, and m is the refractive index of the particle (Zubko *et al.*, 2010). Note that throughout this study, the parameter $kd|m|$ remains less than 0.85.

In general, light scattering by a small particle is determined primarily by the complex refractive index m of the particle material and the ratio of the particle radius expressed as r_{cs} to the wavelength λ: $x = 2\pi r_{cs}/\lambda$ (e.g., Bohren and Huffman, 1983); note, this ratio is referred to as the *size parameter*. While we use the radius of the circumscribing sphere r_{cs} to express particle size, another parameter used is the radius of an equal-volume sphere r_{eq}. We denote the size parameter of the equal-volume sphere as x_{eq} and note that x_{eq} can be derived from x and the average packing density $\langle\rho\rangle$ as follows: $x_{eq} = \langle\rho\rangle^{1/3}x$.

We consider irregularly shaped particles having 3 different refractive indices m, which are representative of materials in cosmic and terrestrial dust: $m = 1.313 + 0i$, $1.6 + 0.0005i$, and $1.5 + 0.1i$. In all these cases, x is varied from 2 to 14 with a fixed step of 2.

2.2.3 Averaging of light scattering characteristics

Light-scattering properties of irregularly shaped particles are averaged over sample shape and orientation at each set of m and x. In all cases, except those of random Gaussian particles, we consider a minimum of 500 sample particle shapes. Light scattering by each sample particle has been computed for one random orientation of the incident electromagnetic wave and averaged over 100 scattering planes evenly distributed around the propagation direction of the incident light. This averaging over scattering planes does not require significant computational efforts; however, it improves significantly the statistical reliability of numerical results.

To test for convergence, we perform averaging in two sub-processes, each based on half of the scattering planes used in each sample (i.e., on 50 scattering planes). We compare results of both sub-processes to the results obtained when averaging over 100 scattering planes. As a quantitative indicator of the averaging, we use the standard deviation of the linear degree of polarization obtained with 100 and 50 scattering planes. This standard deviation depends stochastically on the geometry of light scattering, which could be described, for instance, with phase angle α. Note, α is the angle between two lines, one connecting the source of light to the target particle and the other connecting the target particle to the observer. Obviously, α is equal to 0° in the backscattering direction and 180° in the forward-scattering direction. It also needs to be mentioned that phase angle α is supplementary to the scattering angle θ. We continue averaging over particle shape while fluctuations of the standard deviation of the degree of linear polarization over the entire range of phase angle α exceed 1%; therefore, the actual number of sample particles considered very often exceeds 500.

For the random Gaussian particles, we consider a set of 100 sample particles. Therefore, in order to achieve a desirable accuracy, we consider each sample particle in more than one random orientation of the incident electromagnetic wave. The minimum number of orientations is 5 per sample particle. Although the criterion for termination of the averaging process is the same as for non-Gaussian irregular particles, there is a significant difference: when a given number of orientations of random Gaussian particles does not provide a desirable accuracy of the averaging, we add one additional random orientation for each sample particle from the ensemble and only then check the accuracy again. Therefore, at the termination of the averaging process, light-scattering properties of each sample particle are averaged over the same number of random orientations.

It should be emphasized that while many of the irregularly shaped particles considered in the current review have been studied in Zubko *et al.* (2006; 2007), we have significantly improved the quality of the averaging, so the present results are more statistically reliable. For instance, the minimum number of sample particles used in Zubko *et al.* (2006) was 200; whereas, here it is 500.

2.3 Comparative study of light scattering by irregular particles with different morphology

In general, the parameters describing light scattering by a particle can be classified into two groups, sometimes, referred as integral and differential parameters. For instance, cross-sections for absorption $C_{\rm abs}$ and extinction $C_{\rm ext}$ belong to integral parameters. Simultaneously, intensity I and degree of linear polarization P of the scattered light are examples of differential parameters. An essential feature of integral parameters is that they are independent of the conditions of observation; whereas, differential parameters are functions of two angles specifying the direction of scattered light to a detector. However, in the case of azimuthally symmetric targets, the angular dependence of differential parameters takes a significantly simpler form depending upon only phase angle α or, equivalently, the scattering angle θ. Note that statistically reliable averaging of light-scattering properties over sample particles and/or their orientations obviously makes differential parameters azimuthally averaged; therefore, in this case, the differential parameters also depend upon only one angle.

In the first part of this section, we analyze integral parameters of light scattering by irregularly shaped particles, such as the cross-sections for absorption $C_{\rm abs}$ and extinction $C_{\rm ext}$, single-scattering albedo ω, asymmetry parameter g, and radiation pressure efficiency $Q_{\rm pr}$. Most of these parameters play a key role in the simulation of the transparency of the interstellar medium and radiation transfer in planetary atmospheres including Earth; whereas, the radiation pressure efficiency determines the motion of cosmic dust particles. In the second part of the section, we focus on differential parameters, such as, geometric albedo A, linear and circular polarization ratios $\mu_{\rm L}$ and $\mu_{\rm C}$ at backscattering $\alpha = 0^\circ$, and the dependencies of intensity I and degree of linear polarization P on phase angle α. These parameters are widely exploited in remote sensing applications of atmospheric aerosols, comets and other Solar system bodies.

2.3.1 Comparison of integral parameters of light scattering by irregularly shaped particles with different morphology

2.3.1.1 Cross-sections for absorption $C_{\mathbf{abs}}$ and extinction $C_{\mathbf{ext}}$

Interaction of electromagnetic radiation with particles decreases the energy flux of the incident wave. The total loss of the energy flux can be quantified in terms of area, which is normal to the incident beam and intercepts the lost flux of energy. Such an area is referred to as the cross-section for extinction $C_{\rm ext}$. In the general case, the interaction of electromagnetic radiation with a particle results in absorption and scattering. The part of the total area that corresponds to loss due to absorption is referred to as the cross-section for absorption $C_{\rm abs}$; whereas, the rest corresponds to the cross-section for scattering $C_{\rm sca}$. These three values are obviously related as follows: $C_{\rm ext} = C_{\rm abs} + C_{\rm sca}$.

In Fig. 2.5, we present cross-sections for absorption $C_{\rm abs}$ (left) and extinction $C_{\rm ext}$ (right) as functions of size parameter x for irregularly shaped particles of six different types of morphology. Here, the top panels correspond to the case of $m = 1.313 + 0i$, the middle to $m = 1.6 + 0.0005i$, and the bottom to $m = 1.5 + 0.1i$. Note that, though light scattering by particles comparable with wavelength depends on the dimensionless ratio of particle size to wavelength, $C_{\rm abs}$ and $C_{\rm ext}$ are not dimensionless; they are measured in units of area. For instance, the quantities in Fig. 2.5 are given for wavelength $\lambda = 0.628\,\mu$m (wavenumber $k = 2\pi/\lambda \approx 10$). However, if necessary, they can be easily recalibrated for another λ.

As one can see in Fig. 2.5, except the case of $C_{\rm abs}$ at $m = 1.313 + 0i$, cross-sections for absorption and extinction grow rapidly with size parameter x; whereas, in the case of non-absorbing material, the cross-section for absorption remains predictably equal to zero through all x. Interestingly, curves in Fig. 2.5 reveal qualitatively similar behavior for all types of irregular particles, though there are visible quantitative distinctions. The latter are caused by differences in morphology and material volume between various types of irregularly shaped particles. On the other hand, for equidimensional target particles at small x, one could expect that the impact of particle morphology on light scattering has to be rather small because, in this case, light-scattering properties can be described quite well with only an isotropic electric dipole (e.g., Bohren and Huffman, 1983). However, the upper limit for the range of x where $C_{\rm abs}$ and $C_{\rm ext}$ are insensitive to morphology is unknown and, thus, its determination is of high practical interest.

In order to eliminate the impact of different volumes of material, one can consider ratios $C_{\rm abs}/\langle\rho\rangle$ and $C_{\rm ext}/\langle\rho\rangle$ instead of pure cross-sections for absorption and extinction. These normalized quantities are shown in Fig. 2.6. As one can see, agreement between different types of irregularly shaped particles becomes much better, namely, all curves nearly coincide, at least for $x \leq 4$. Moreover, in some cases, the coincidence is extended to much larger x. Particularly, the extinction cross-section of icy particles (i.e., $m = 1.313 + 0i$) does not depend on their morphology for $x \leq 8$. Interestingly, the differential parameters of light scattering, such as the angular profiles of intensity I and degree of linear polarization P, reveal significant deviations depending on morphology at $m = 1.313 + 0i$ and $x = 6$ (see top panels in Fig. 2.10). Surprisingly, in the case of weak absorption, the absorption cross-section

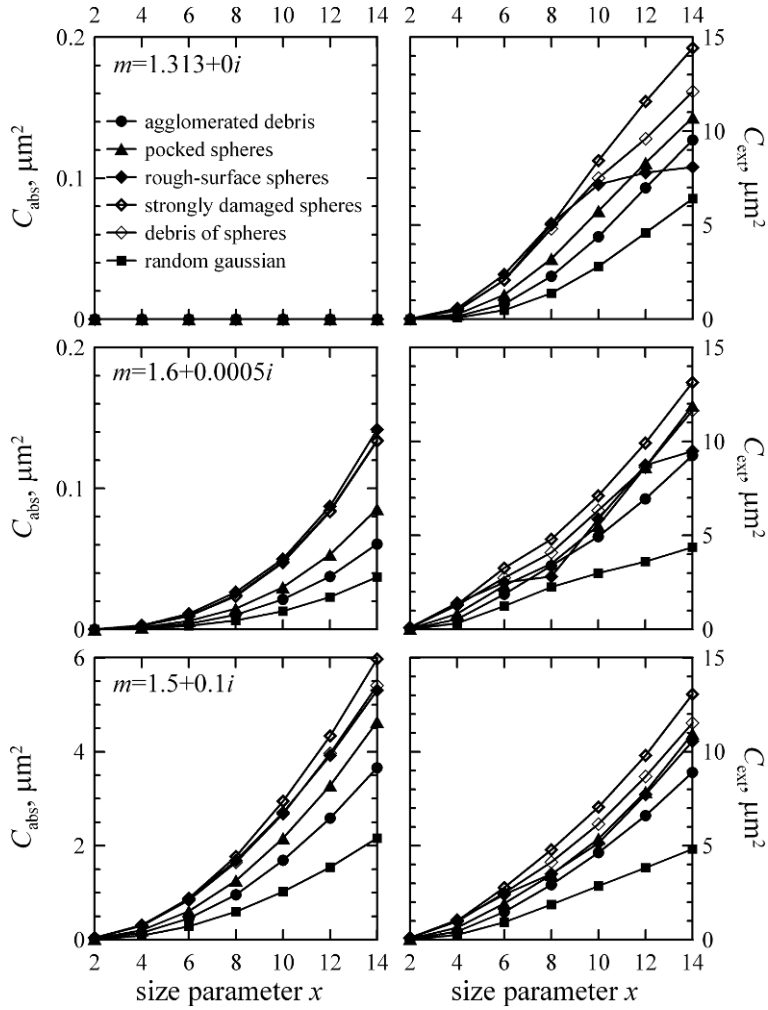

Fig. 2.5. Cross-sections for absorption $C_{\rm abs}$ (left) and extinction $C_{\rm ext}$ (right) computed at $\lambda = 0.628\,\mu$m, as functions of size parameter x for six types of irregularly shaped particles. The top panels show the case of $m = 1.313 + 0i$, the middle panels show the case of $m = 1.6 + 0.0005i$, and the bottom panels show the case of $m = 1.5 + 0.1i$.

remains insensitive to particles morphology over the entire range of x investigated in the current work (see left middle panel in Fig. 2.6).

Finally, we would like to note that within each morphology class of irregular particles, the cross-section for extinction $C_{\rm ext}$ attains similar absolute values at $m = 1.5 + 0.1i$ and $m = 1.6 + 0.0005i$ (see Figure 5). One can conclude that the imaginary part of refractive index $\mathrm{Im}(m)$ does not significantly affect $C_{\rm ext}$. Therefore, considerable extinction of radiation does not necessarily mean the presence of highly absorbing particles. However, $\mathrm{Im}(m)$ has a significant impact on absorption cross-section $C_{\rm abs}$, and therefore also on the scattering cross-section $C_{\rm sca}$.

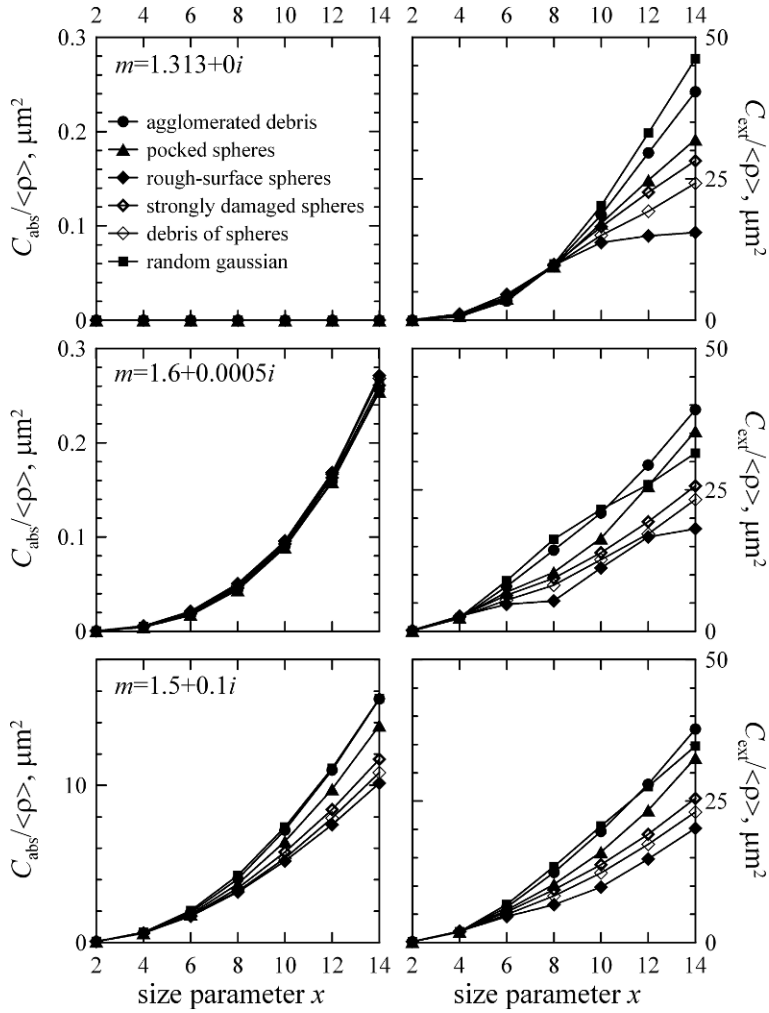

Fig. 2.6. The same as Fig. 2.5 but, C_{abs} and C_{ext} are normalized to an average packing density $\langle\rho\rangle$ of irregularly shaped particles.

2.3.1.2 Single-scattering albedo ω and asymmetry parameter g

Fig. 2.7 shows another pair of integral parameters of light scattering, namely, single-scattering albedo ω and asymmetry parameter g. The former is defined as the ratio $\omega = C_{\text{sca}}/C_{\text{ext}} = (C_{\text{ext}} - C_{\text{abs}})/C_{\text{ext}}$; it varies from 0 and to 1 and presents a sort of efficiency of light scattering. The parameter g indicates the distribution of the scattered electromagnetic energy between forward and backward hemispheres with respect to the direction of the incident beam propagation:

$$g = \frac{\int\limits_{2\pi}\int\limits_{\pi} I(\theta,\varphi)\,\cos\theta\,\sin\theta\,d\theta\,d\varphi}{\int\limits_{2\pi}\int\limits_{\pi} I(\theta,\varphi)\,\sin\theta\,d\theta\,d\varphi}\,. \tag{1}$$

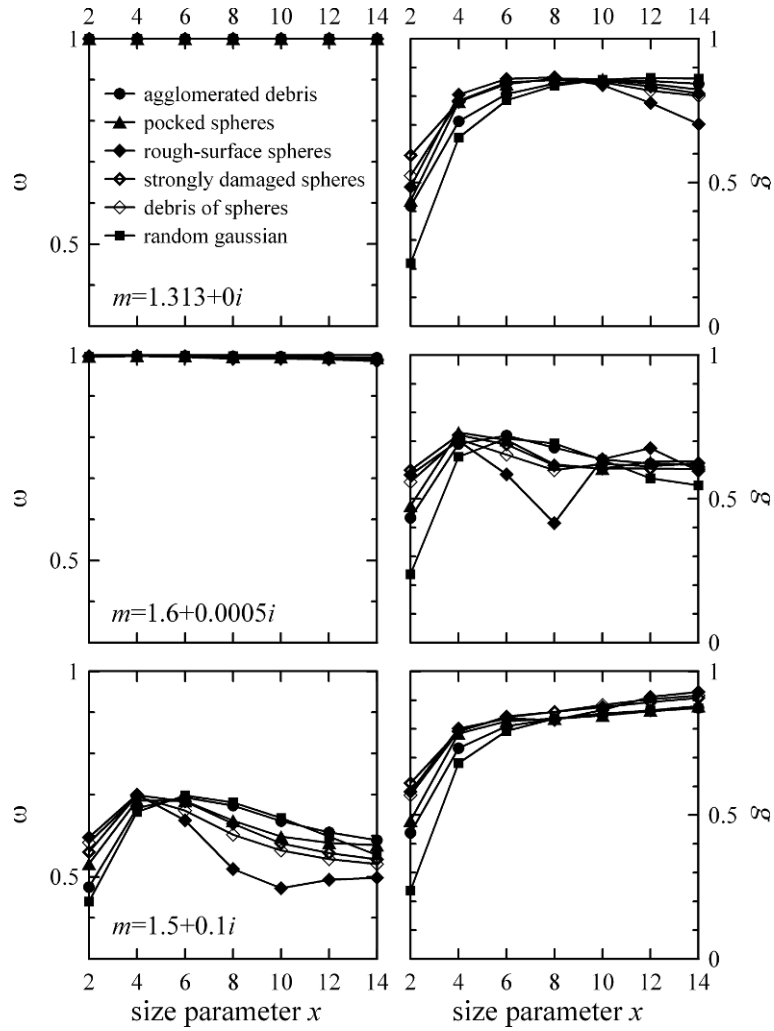

Fig. 2.7. Single-scattering albedo ω (left) and asymmetry parameter g (right) as a function of size parameter x for six types of irregularly shaped particles. The top panels show the case of $m = 1.313 + 0i$, the middle panels show the case of $m = 1.6 + 0.0005i$, and the bottom panels show the case of $m = 1.5 + 0.1i$.

Here, θ and φ are the scattering and azimuthal angles, $I(\theta, \varphi)$ is the intensity of scattering of unpolarized light. The denominator is equal to the scattering cross-section $C_{\rm sca}$. Note that scattering intensity is a function of two angles in the general case; whereas, averaging over sample particles and/or their orientation removes the dependence on azimuthal angle φ. Asymmetry parameter g varies in the range from -1 to 1. It takes a positive value if the scattering into the forward hemisphere dominates over that into backward hemisphere, and $g = 0$ if the energy is distributed equally between hemispheres and is negative otherwise. Note that both single-scattering albedo ω and asymmetry parameter g are important parameters

in computations of radiative transfer in discrete media (e.g., Bowell *et al.*, 1989; Bauer *et al.*, 2007).

As one could expect, single-scattering albedo ω of non-absorbing particles is exactly equal to unity. This means that all incident electromagnetic energy intercepted by a target particle is being scattered into surrounding space (see Fig. 2.7). However, a small imaginary part of refractive index $\mathrm{Im}(m) = 0.0005$ does not significantly affect ω either; for instance, the albedo remains higher than 98.5% for all types of particles and sizes. In case of highly absorbing material with $\mathrm{Im}(m) = 0.1$, there is a significant dependence of ω on x. Nevertheless, for the case of $m = 1.5 + 0.1i$ shown in Fig. 2.7, all profiles ω vs. x are quite similar to each other. Namely, in the range of x from 2 to 4–6, single-scattering albedo grows rapidly with size parameter x; then, it slowly decreases. Note that ω remains higher than 0.4 through all cases considered.

Interestingly, except in the case of rough-surface spheres, there is quite good quantitative agreement between albedo ω of particles with different morphologies. On the other hand, as was shown in Zubko *et al.* (2006), light scattering by the rough-surface spheres is very close to that of a perfect sphere of equivalent volume. Therefore, one may conclude, once irregular particles substantially differ from a perfect sphere, their single-scattering albedo ω does not depend significantly on their morphology. This statement is consistent with findings in Nousiainen and Muinonen (2007), where random Gaussian spheres having appreciably different shapes were studied. Nevertheless, in the case of irregular particles with some specific morphologies, such as extremely sparse ballistic cluster–cluster aggregates (BCCAs) and ballistic particle–cluster aggregates (BPCAs), the size dependence of single-scattering albedo ω may be substantially different from the profiles shown in Fig. 2.7. Notice, there is quite good quantitative agreement between single-scattering albedo of BCCAs and BPCAs (Kimura and Mann, 1998).

As one can see in the right panels of Fig. 2.7, the asymmetry parameter g shows more or less the same dependence on the size parameter x for all types of irregularly shaped particles. Note that, as in the case of single-scattering albedo ω, the most notable deviations from the general behavior are caused by rough-surface spheres. These deviations become apparent in cases of non- and weakly absorbing materials; whereas, in the case of $m = 1.5 + 0.1i$, rough-surface spheres do not reveal visible distinctions from the behavior of irregular particles with other morphologies.

Interestingly, irregular particles with different degrees of absorption reveal visibly different trends of curves g vs. x. Indeed, as one can see in Fig. 2.7, curves corresponding to weakly absorbing particles show a maximum at $x \approx 10$–12 ($m = 1.313 + 0i$) and $x \approx 4$–6 ($m = 1.6 + 0.0005i$). Note that similar non-monotonic behavior was found for particles with regular structure (Mishchenko, 1994; Bauer *et al.*, 2007), although in the case of irregular particles the maximum is located at systematically higher x. Simultaneously, profiles for highly absorbing particles approach the level $g = 1$ asymptotically, having no extremum. This behavior is also consistent with findings for spheres with large material absorption (Mishchenko, 1994). However, in this case, there is also rather good quantitative agreement between asymmetry parameters g for spheres and irregular particles.

We would like to note that the sign of the asymmetry parameter g for all six types of irregular particles is positive throughout the entire range of size parameter

x considered in Fig. 2.7. In practice this means that the amount of electromagnetic energy scattered in the forward hemisphere is greater than that scattered in the backward hemisphere. This result is consistent with findings for other types of particles, such as single spheres, randomly oriented oblate spheroids and Chebyshev particles (Mishchenko, 1994), particles with multiple internal inclusions (Macke and Mishchenko, 1996), BCCA and BPCA (Kimura and Mann, 1998), and layered spheres (Bauer *et al.*, 2007).

Putting a target particle into some electromagnetic field disturbs its initial structure. In order to express analytically the resulting (i.e., disturbed) electromagnetic field in space with respect to the particle, it is assumed that the total electromagnetic field is the sum of the initial electromagnetic field (i.e., the field existing in the absence of the obstacle) and the scattered electromagnetic field (i.e., all the rest). As it turns out, such a decomposition of the electromagnetic field in space is quite convenient for a subsequent analysis of electromagnetic scattering (Bohren and Huffman, 1983). However, in what follows, only the scattered electromagnetic field is studied; whereas, the incident electromagnetic field is ignored. Note that the definition of g eq. (1) presents exactly this case. Evidently, omitting the incident field corresponds to the case when the detector of radiation is isolated from the direct incident electromagnetic field. While this occurs in the vast majority of experiments and observations of light scattering, it does not hold true in the case of multiple scattering between closely packed particles. Indeed, in this case, the detector is a neighboring particle, which is irradiated by not only the electromagnetic wave scattered from the target particle but by the incident wave as well. Therefore, when considering the asymmetry parameter g for constituent particles forming a discrete medium, the intensity of scattering in relationship (1) has to be replaced with the intensity of the full electromagnetic field, which is based on the amplitude of the full electromagnetic field. Therefore, one can summarize that data for asymmetry parameter g shown in Fig. 2.7 can be used only in applications to single-scattering particles or constituents of clusters with very sparse and random structure; whereas, in the case of closely packed clusters, asymmetry parameter g needs to be computed in a way different from eq. (1).

2.3.1.3 Efficiency for radiation pressure Q_{pr}

The radiation-pressure efficiency Q_{pr} determines the motion of cosmic dust particles. It is defined as follows:

$$Q_{\mathrm{pr}} = C_{\mathrm{pr}}/G = (C_{\mathrm{ext}} - gC_{\mathrm{sca}})/G. \tag{2}$$

Here, G is the geometric cross-section of the particle and C_{pr} is the cross-section for radiation pressure (e.g., van de Hulst, 1981); whereas, C_{ext}, C_{sca}, and g are, as given previously, the cross-sections for extinction and scattering, and asymmetry parameter, respectively. Note that the motion of cosmic dust particles near a star depends on the ratio of the radiation-pressure force to the star's gravitational force, which is designated as β (e.g., Burns et al., 1979; Artymowicz, 1988; Fulle, 2004). Some details on the difference between the orbit of the parent body and an ejected dust particle caused by radiation pressure acting on the particle can be found, e.g., in Augereau and Beust (2006). By definition, the ratio β is in direct proportion to

radiation pressure: $\beta \propto Q_{\rm pr}$ (e.g., Fulle, 2004). However, there is an obvious lack of $Q_{\rm pr}$ data for irregularly shaped particles. For most applications, computations of β are based on the radiation-pressure efficiency of a single sphere obtained using Mie theory (Burns et al., 1979; Artymowicz, 1988; Fulle, 2004; Augereau and Beust, 2006). Nevertheless, in some cases, particles with more complicated structure have been considered, such as, BCCA and BPCA clusters (Kimura and Mann, 1998; Kimura et al., 2002) or layered spheres (Wickramasinghe and Wickramasinghe, 2003).

In Fig. 2.8, we present radiation-pressure efficiencies $Q_{\rm pr}$ vs. size parameter x of irregularly shaped particles having six different types of morphology. One can immediately conclude that particles with $m = 1.313 + 0i$ behave peculiarly. In

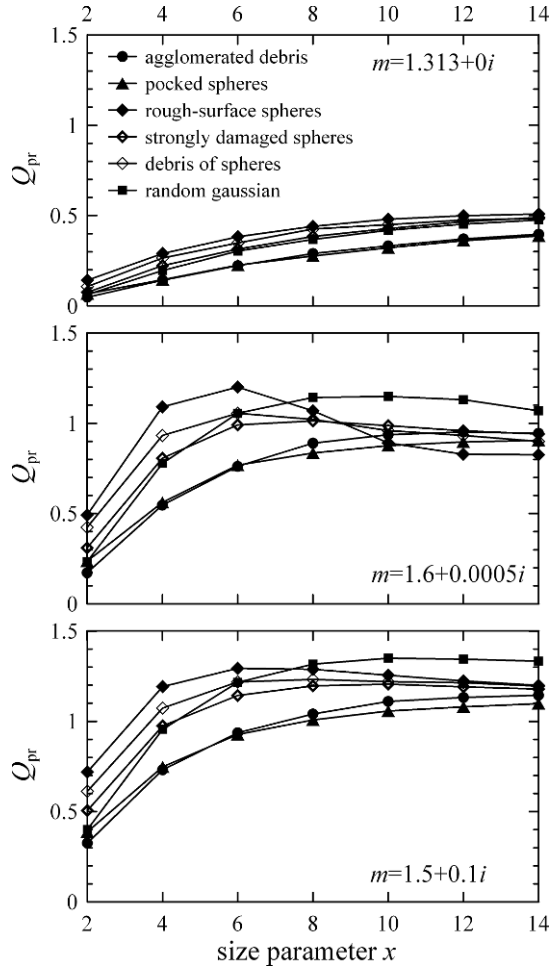

Fig. 2.8. Radiation-pressure efficiency $Q_{\rm pr}$ (i.e., the ratio of radiation pressure cross-section $C_{\rm pr}$ to geometric cross-section G) as a function of size parameter x for six types of irregularly shaped particles. The top panels show the case of $m = 1.313 + 0i$, the middle panels show the case of $m = 1.6 + 0.0005i$, and the bottom panels show the case of $m = 1.5 + 0.1i$.

comparison to this case, values of $Q_{\rm pr}$ for particles with $m = 1.6 + 0.0005i$ and $m = 1.5 + 0.1i$ are surprisingly close to each other; although radiation-pressure efficiency for highly absorbing particles systematically exceeds that for weakly absorbing particles. Interestingly, through all the studied refractive indices m and size parameters x, $Q_{\rm pr}$ for agglomerated debris particles and pocked spheres nearly coincide with each other. Both types of particles have fluffy irregular structure but with different packing densities. Quantitative resemblance also can be seen between curves for strongly damaged spheres and debris of spheres; whereas, rough-surface spheres and Gaussian random particles show individual dependences of $Q_{\rm pr}$ on x.

Note that in numerous practical applications, it is assumed that $Q_{\rm pr} \approx 1$ for very large particles with sizes significantly exceeding 1 μm (e.g., Burns et al., 1979; Fulle, 2004). However, as one can see in Fig. 2.8, while increasing size parameter x, the radiation-pressure efficiency $Q_{\rm pr}$ of non-optically soft irregular particles clearly approaches 1. For instance, at the largest size parameter $x = 14$ achieved in this study, the relative deviations of $Q_{\rm pr}$ from 1 do not exceed 20–25%; whereas, in the case of particles with fluffy structure (i.e., agglomerated debris particles and pocked spheres), these deviations are even smaller. Therefore, in the case of non-optically soft irregular particles, the efficiency for radiation pressure $Q_{\rm pr}$ can be assumed approximately equal to 1 when the particle size is larger than only a few micrometers in visible.

2.3.2 Comparison of differential parameters of light scattering by irregularly shaped particles with different morphology

There are a few different ways to describe properties of the scattered electromagnetic radiation. One of them is the formalism of the four-dimensional *Stokes vector*:

$$\boldsymbol{S} = \begin{pmatrix} I \\ Q \\ U \\ V \end{pmatrix}. \tag{3}$$

In eq. (3), the Stokes parameter I represents the total intensity of the electromagnetic wave, the Stokes parameters Q and U describe its linear polarization with respect to a given scattering plane, e.g., the plane containing the source of incident light, target particle, and observer; finally, the Stokes parameter V characterizes circular polarization of the electromagnetic wave. The most important advantage of such an approach is the simplicity in representation of the natural unpolarized light. Indeed, a monochromatic electromagnetic wave is polarized always 100%; whereas, unpolarized electromagnetic radiation appears as a superposition of numerous completely but stochastically polarized waves. However, for instance, within formalism based on amplitude and phase of electromagnetic wave, it is practically impossible to represent unpolarized light; whereas, in terms of the Stokes vector it can be quite easily expressed as follows:

$$\boldsymbol{S} = \begin{pmatrix} I \\ 0 \\ 0 \\ 0 \end{pmatrix}, \tag{4}$$

i.e., in the case of unpolarized light, the Stokes parameters Q, U, and V are assumed to be equal to zero. For convenience, the intensity of the incident light is assumed very often to be equal to 1.

Within the formalism of the Stokes vectors, the act of light scattering by a particle can be described with the help of a matrix–vector product $\mathbf{S}^{sc} = \mathbf{M}\mathbf{S}^{inc}$. Here, $\mathbf{S}^{inc}$ and $\mathbf{S}^{sc}$ are Stokes vectors for the incident and scattered light, respectively; whereas, $\mathbf{M}$ denotes a special 4×4 matrix, which describes the light-scattering properties of the target particle. Note that this matrix contains all possible differential parameters of light scattering. It is called the *Mueller matrix* (e.g., van de Hulst, 1981; Bohren and Huffman, 1983) and sometimes the *scattering matrix* (Bohren and Huffman, 1983). In general, all sixteen elements of the Mueller matrix are nonzero and depend on phase angle α.

It should be emphasized that the Stokes vector and the Mueller matrix are both specified within a given scattering plane. In order to obtain the actual values of the Mueller matrix elements for a given target particle and a given scattering plane, it is necessary to compute the electromagnetic scattering by that particle for two incident waves having orthogonal polarization states. The complete Mueller matrix can be derived from the resulting scattered fields with the help of simple formulae presented, e.g., in Bohren and Huffman (1983). Note that a change of the scattering plane, for instance, caused by rotation of the target particle around the direction of incident wave propagation, requires a complete recalculation of the Mueller matrix. In other words, the Mueller matrix of a single particle corresponding to one scattering plane cannot be easily transformed to the Mueller matrix associated with another scattering plane. Nevertheless, this procedure can be substantially accelerated owing to the linearity of Maxwell equations.

Averaging of light-scattering properties over sample particles and their orientations substantially simplifies the resulting Mueller matrix. In particular, half of the elements in the average Mueller matrix are equal to zero; whereas, some of the nonzero elements are not independent. In general, the average Mueller matrix takes on the following form (e.g., van de Hulst, 1981):

$$\mathbf{M} = \frac{1}{(kR)^2} \begin{pmatrix} M_{11} & M_{12} & 0 & 0 \\ M_{12} & M_{22} & 0 & 0 \\ 0 & 0 & M_{33} & M_{34} \\ 0 & 0 & -M_{34} & M_{44} \end{pmatrix}. \tag{5}$$

As one can see in (5), there are only six truly independent elements, although this number can be even less in the case of some special target particles. For instance, the Mueller matrix for a sphere consists of four independent elements; whereas $M_{11} = M_{22}$ and $M_{33} = M_{44}$ (Bohren and Huffman, 1983). When defining the Mueller matrix, it is common to distinguish the factor $(kR)^{-2}$, which describes the energy attenuation of the spherical wave with distance R and is common for all elements of the matrix (Bohren and Huffman, 1983).

In practice, when measuring light scattering by micron-sized particles, a cumulative signal coming simultaneously from enormous numbers of particles, is registered. Except in a few quite specific cases (e.g., Rosenbush et al., 2007), these particles are randomly oriented. Therefore, the form of the matrix retrieved in practice usually takes the form of eq. (5) (e.g., Muñoz et al., 2000; Hovenier et al., 2003; Volten

et al., 2007). In astronomical applications, the incident light typically is emitted by some star, and such electromagnetic radiation is substantially unpolarized. As a consequence, the light-scattering parameters which are most commonly available in astronomical observations are defined by product of the Mueller matrix (eq. (5)) and the Stokes vector (eq. (4)), i.e.:

$$\mathbf{S}^{sc} = \frac{1}{(kR)^2} \begin{pmatrix} M_{11} \\ M_{12} \\ 0 \\ 0 \end{pmatrix}. \tag{6}$$

Obviously, the Stokes vector (6) remains valid for passive measurements of light scattering by atmospheric aerosols, i.e., with the Sun as the source of light (e.g., Kokhanovsky, 2008).

As one can see in (6), there are only two nonzero Stokes parameters containing information. However, the commonly measured values are the intensity of the scattered light $I = (kR)^{-2} M_{11}$ and its degree of linear polarization $P = -M_{12}/M_{11}$. Typically polarization is expressed in percent. Note that, taking into account the definitions for the Mueller matrix elements M_{11} and M_{12} (Bohren and Huffman, 1983), one can reformulate definitions for the intensity and degree of linear polarization alternatively as follows: $I = I_{\perp} + I_{||}$ and $P = (I_{\perp} - I_{||})/(I_{\perp} + I_{||})$. Here, $I_{\perp}$ denotes the intensity of the component of scattered light that is polarized perpendicular to the scattering plane; whereas, $I_{||}$ denotes the intensity of the component polarized within the scattering plane. While intensity I always takes positive and nonzero values, the degree of linear polarization P can take positive and negative values and also be equal to zero. Note also that sometimes the dependence of intensity I on phase angle α, which is normalized to the scattering cross-section $C_{\rm sca}$, is called the *phase function* (e.g., van de Hulst, 1981; Bohren and Huffman, 1983; Kokhanovsky, 2008).

2.3.2.1 Full phase dependencies of the intensity and degree of linear polarization

Figs. 2.9–2.12 show the phase dependencies of intensity I normalized to its value at the backscattering (left) and degree of linear polarization P (right) for particles with size parameter $x = 2$, 6, 10, and 14, correspondingly. The upper panels show the results for particles with $m = 1.313 + 0i$, results with $m = 1.6 + 0.0005i$ are shown in the middle, and results with $m = 1.5 + 0.1i$ are shown in the bottom. For all the refractive indices presented in Fig. 2.9, the phase dependencies of intensity are not symmetric, having a wide peak of forward scattering. The intensity of forward scattering is up to about two orders of magnitude higher than that of bsackscattering; however, in the case of optically soft particles with $m = 1.313 + 0i$, this difference is less pronounced. As one can see in Fig. 2.9, even the smallest particles with $x = 2$ reveal noticeable differences in the intensity depending upon the particle morphology. On the other hand, curves for particles with similar morphology are generally in good quantitative agreement. For instance, the intensity profiles for agglomerated debris particles and pocked spheres are quite similar to

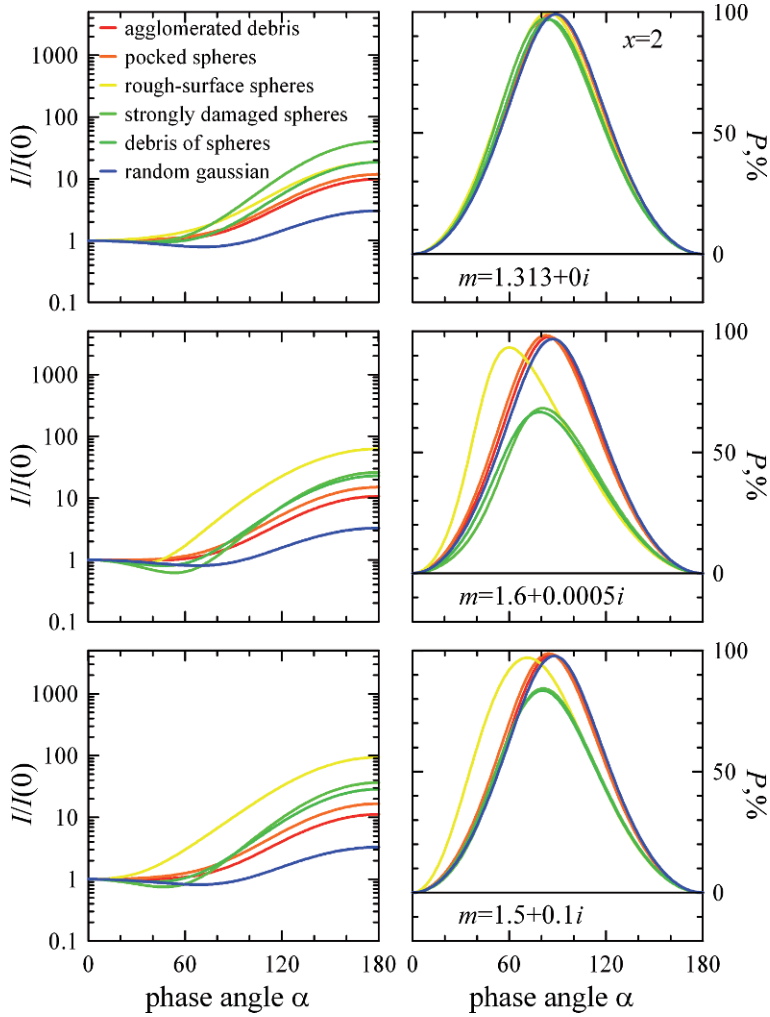

Fig. 2.9. Intensity I (left) and degree of linear polarization P (right) as functions of phase angle α for six types of irregularly shaped particles with $x = 2$. The top panels show the case of $m = 1.313 + 0i$, the middle panels show the case of $m = 1.6 + 0.0005i$, and the bottom panels show the case of $m = 1.5 + 0.1i$.

each other for all refractive indices studied. The same is observed for strongly damaged spheres and debris of spheres, except the case of $m = 1.313 + 0i$. We would like to emphasize that such similarities remain in the angular profiles of the degree of linear polarization (see right panels in Fig. 2.9) for agglomerated debris particles and pocked spheres, and for strongly damaged spheres and debris of spheres.

As one can see in Fig. 2.9, the degree of linear polarization, for all types of irregular particles with $x = 2$, remains substantially positive through all phase angles and refractive indices. The phase curves of linear polarization have a bell-like shape. In most cases, the maximum of positive polarization is located near $\alpha = 90°$; and only in the case of the rough-surface spheres, the maximum of linear polarization

is noticeably shifted toward smaller phase angles. Through all the cases considered in Fig. 2.9, the maximum amplitude of linear polarization exceeds 60%; however, in many cases, the amplitude is even higher, reaching almost 100%. For instance, at $m = 1.313 + 0i$, all irregularly shaped particles have a very high maximum linear polarization. Such angular profiles of linear polarization nearly coincide with the result of the *Rayleigh approximation* for an extremely small particle, i.e., with $x \ll 1$ (e.g., van de Hulst, 1981; Bohren and Huffman, 1983). On the other hand, the Rayleigh approximation also predicts a symmetric phase function of small particles, which is not observed for the irregular particles with $x = 2$. Therefore, one can conclude that, in the case of small size parameter x, the angular dependence of the intensity is considerably more sensitive to particles' morphology than the degree of linear polarization. Interestingly, while the size of the particles grows, becoming comparable with the wavelength, the degree of linear polarization becomes more sensitive to properties of particles than the intensity (e.g., Zubko *et al.*, 2007; Nousiainen, 2009).

Fig. 2.10 shows phase dependencies of intensity I and degree of linear polarization P for irregular particles of $x = 6$. There is a dramatic difference from the curves for $x = 2$ presented in Fig. 2.9. The forward-scattering peak is substantially narrower in the case of $x = 6$. For optically soft and highly absorbing particles, the difference between intensities in the forward and backward scattering is an order of magnitude higher than for $x = 2$; however, in the case of $m = 1.6 + 0.0005i$, this difference is not so great. Unlike for the case of $x = 2$, angular profiles of the intensity and degree of linear polarization are accompanied with oscillations, which are most apparent for rough-surface spheres. The locations of these oscillations are close with those of the corresponding equal volume sphere (Zubko *et al.*, 2006). Among morphologies considered through this study, particles with agglomerated structure (i.e., agglomerated debris particles and pocked spheres) show the smoothest overall profiles of the intensity and degree of linear polarization. Moreover, as for $x = 2$, one can see quite good quantitative agreement between the curves corresponding to these two types of particles. Interestingly the similarities between strongly damaged spheres and debris of sphere, which are found for small particles with $x = 2$, do not seem to be present for $x = 6$.

Weakly absorbing particles reveal enhancement of the intensity near backscattering $\alpha = 0°$; whereas, in case of highly absorbing particles, the intensity curve is flattened around $\alpha = 0°$. In general, the enhancement of intensity near backscattering correlates qualitatively with the *negative polarization branch* (NPB), which also appears at small phase angles (see right panels in Fig. 2.10). Nevertheless, a quantitative interrelation between the enhancement of intensity near backscattering and the NPB does not take a simple form. For instance, at $m = 1.6 + 0.0005i$, the enhancement of intensity produced by rough-surface spheres does not significantly differ from that for strongly damaged spheres. However, NPBs of these particles diverge dramatically. One can see also that the width of the intensity surge near backscattering does not correlate unambiguously with the width of the NPB. Finally, there exists a dramatic decrease of the NPB due to the high absorption. Indeed, particles of all morphologies with $m = 1.5 + 0.1i$ almost do not show NPB.

Fig. 2.11 shows the phase curves of intensity I and degree of linear polarization P for particles with $x = 10$. As one can see, the further increase of particles size

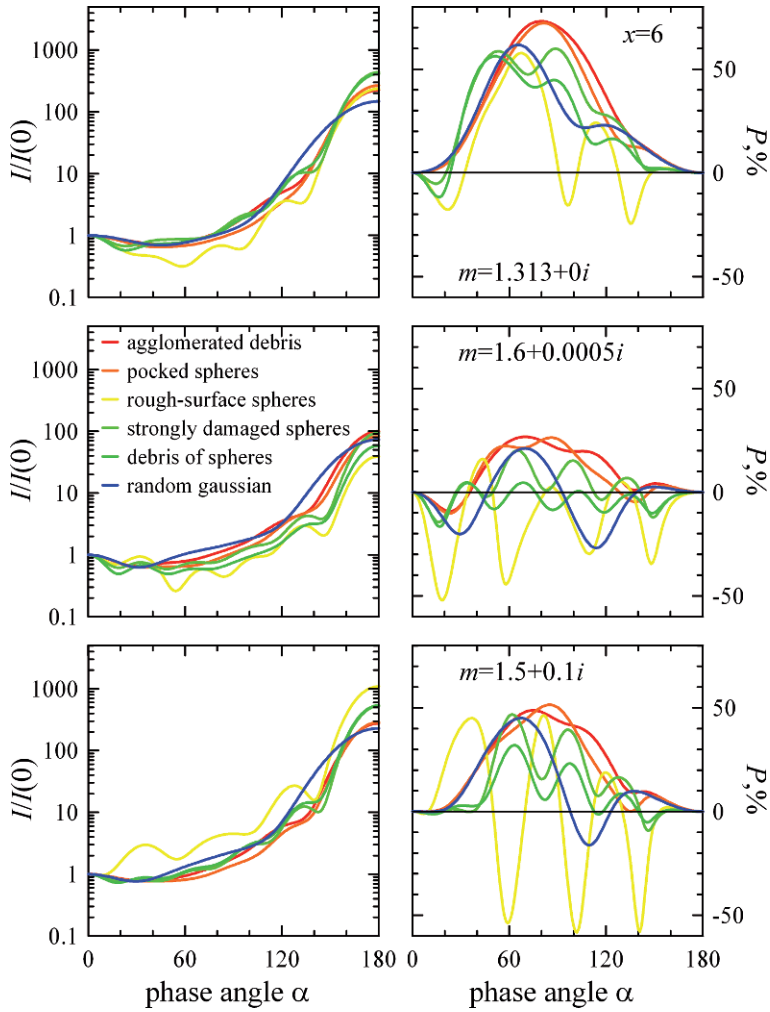

Fig. 2.10. The same as Fig. 2.9 but, for $x = 6$.

causes changes in the curves of intensity and linear polarization, which generally are consistent with those previously found between $x = 2$ and 6; however, they are much less dramatic. The smaller impact of size increase can be explained as follows. The growth of x from 2 to 6 equates to a threefold increase of particle size; whereas, the change from $x = 6$ to 10 equates to less than a twofold increase. The most noticeable change in light-scattering properties concerns the oscillations on phase curves of intensity and polarization. Indeed, in the case of $x = 10$, their number is significantly higher than at $x = 6$; simultaneously, the amplitude of oscillations is substantially damped, though, for rough-surface spheres, the oscillations remain quite dramatic in appearance.

It is interesting to compare the phase dependencies of intensity and polarization for rough-surface spheres and random Gaussian particles presented in Figs. 2.10–2.12. As was previously mentioned, these are two types of particles having compact

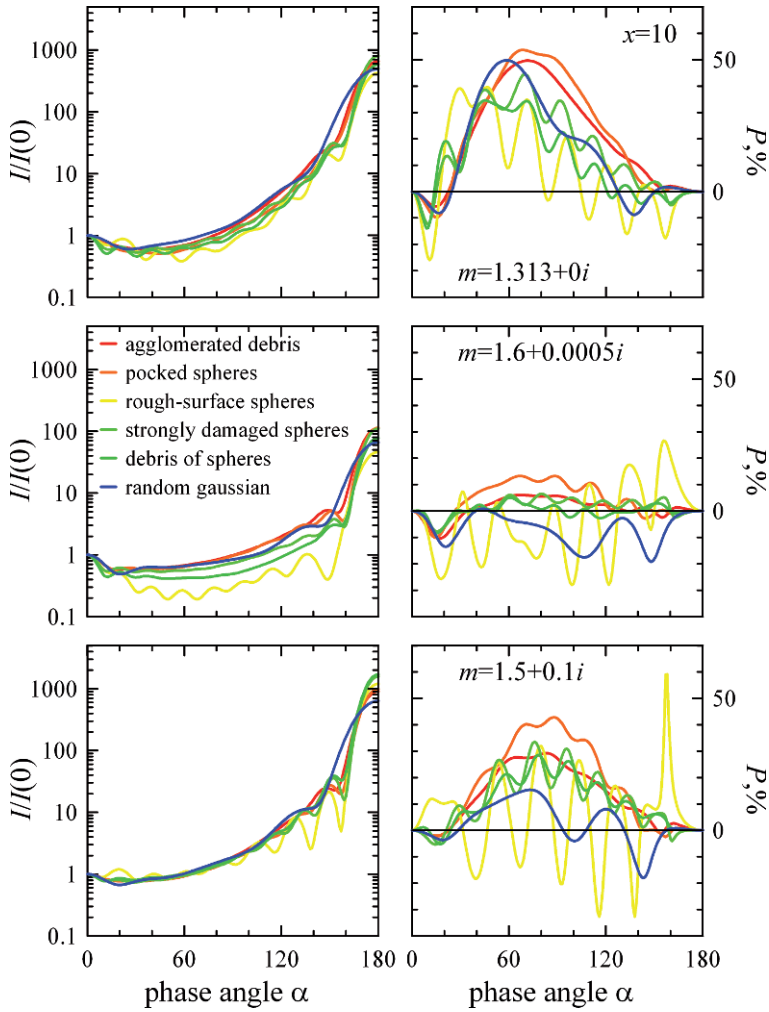

Fig. 2.11. The same as Fig. 2.9 but, for $x = 10$.

morphology. However, rough-surface spheres have an overall shape that is more or less spherical, but with significant surface roughness. The overall shape of a random Gaussian particle differs significantly from that of a sphere, yet its surface remains quite smooth (see in Fig. 2.3). As one can see, the phase curves of intensity and degree of linear polarization for rough-surface spheres reveal visibly more oscillatory behavior than random Gaussian particles. One can conclude that overall nonsphericity in particle shape is more efficient at eliminating light-scattering resonances than the surface roughness.

As one can see in Fig. 2.11, there is not a systematic resemblance between curves for agglomerated debris particles and pocked spheres with $x = 10$, like that seen for $x = 2$ and 6. Except for the angular profile of intensity for $m = 1.5+0.1i$, irregularly shaped particles with different morphology produce completely distinctive phase

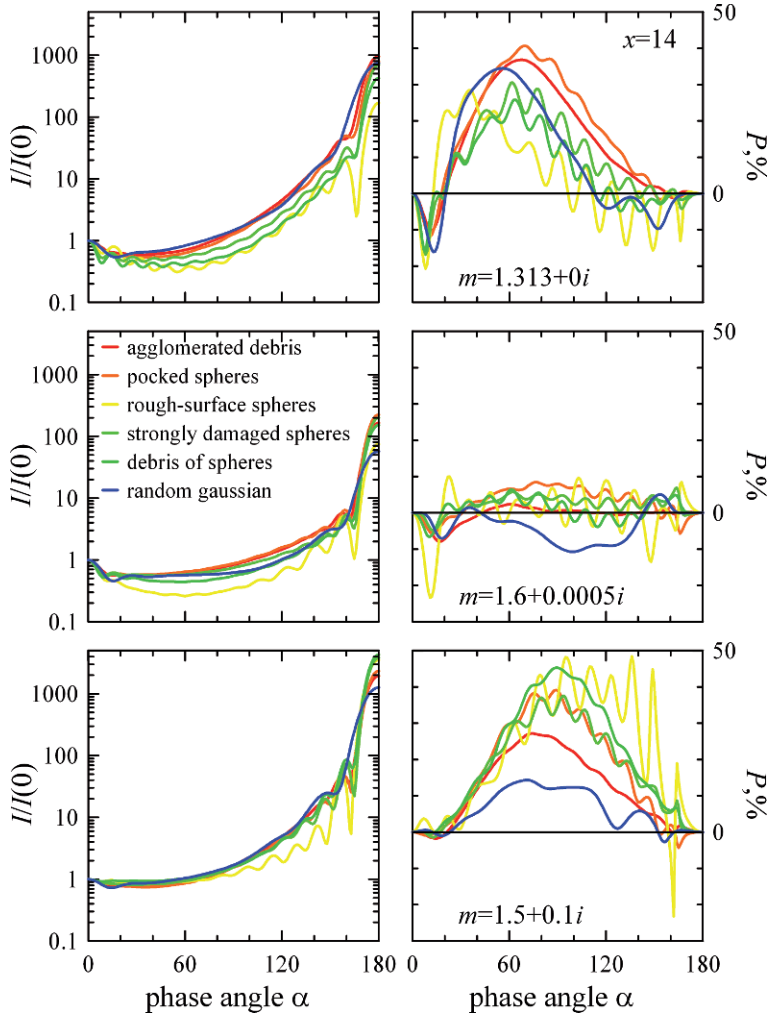

Fig. 2.12. The same as Fig. 2.9 but, for $x = 14$.

dependencies of intensity and degree of linear polarization at $x = 10$. Note that in Fig. 2.12, the same conclusions are valid for the case of $x = 14$.

Except for the case of rough-surface spheres with $m = 1.5 + 0.1i$, all irregular particles with $x = 10$ show a noticeable enhancement of intensity near backscattering and a NPB. Manifestation of both effects is visibly damped in highly absorbing particles. Note that, in the case of $x = 10$, as well as $x = 6$, the shape of the NPB is visibly non-symmetric, as the minimum of polarization is shifted toward the inversion point of polarization sign, i.e., $P(\alpha \neq 0^\circ) = 0\%$, rather than toward $\alpha = 0^\circ$. This kind of non-symmetry in shape of NPB has been found for other non-spherical particles with $x < 10$ (e.g., Lumme *et al.*, 1997; Zubko *et al.*, 2001; 2003; 2004; 2006; 2007; Kimura and Mann, 2004; Vilaplana *et al.*, 2006; Muinonen *et al.*, 2007; Nousiainen and Muinonen, 2007; Lindqvist *et al.*, 2009; Shen *et al.*,

2009). For weakly absorbing particles, while size parameter x increases, the NPB tends to become more symmetric (e.g., Zubko et al., 2004; 2006). This effect can be observed in Fig. 2.12. Note that further growth of particle size can make the shape of the NPB again non-symmetric but inversely to that of $x < 10$; for instance, in Fig. 2.12, consider the curve for agglomerated debris particles with $x = 14$ and $m = 1.6 + 0.0005i$. For highly absorbing particles, an increase of x does not significantly affect the symmetry of the NPB. However, it may cause a small additional branch of positive polarization near $\alpha = 0°$. Examples of such angular profiles of the NPB can be found for debris of spheres at $x = 10$ and $m = 1.5+0.1i$ (Fig. 2.11) or for a few types of particles with $x = 14$ and $m = 1.5+0.1i$ (Fig. 2.12). Note that, this additional positive polarization branch near backscattering also was found in other numerical simulations of light scattering by finite targets (see also Videen, 2002; Zubko *et al.*, 2009a); it seems that the effect appears predominately in the case of weak NPB.

Finally, we consider the rather deep negative polarization (up to -20%) produced by random Gaussian particles with $x = 10$–14 and $m = 1.6 + 0.0005i$, which is located at intermediate phase angles (see, Figs. 2.11 and 2.12). Interestingly, the presence of the negative polarization under given phase angles was also found in laboratory measurements of rutile (Muñoz *et al.*, 2006); whereas, an exhaustive explanation of this effect has been recently proposed by Tyynelä *et al.* (2010).

2.3.2.2 Parameters $P_{\min}$, $\alpha_{\min}$, $P_{\max}$, and $\alpha_{\max}$, describing the angular profile of degree of linear polarization

The angular dependence of the degree of linear polarization observed for the Moon (e.g., Dollfus and Bowell, 1971; Shkuratov *et al.*, 1992; Shkuratov and Opanasenko, 1992), asteroids (e.g., Zellner and Gradie, 1976), comets (e.g., Kiselev and Chernova, 1981; Chernova *et al.*, 1993), and zodiacal light (e.g., Dumont and Sanchez, 1975; Levasseur-Regourd *et al.*, 1990) consists of two prominent features: the NPB at small phase angles and a positive polarization branch (PPB) in the remaining range of phase angles. Transition of NPB to PPB happens at the *inversion angle* α_{inv}, which varies from 15°, in the cases of F-type asteroids (Belskaya *et al.*, 2005) and nucleus of comet 2P/Enke (Boehnhardt *et al.*, 2008), up to 30° in cases of circumnuclear haloes of various comets (Hadamcik and Levasseur-Regourd, 2003) and asteroid 234 Barbara (Cellino *et al.*, 2006). Simultaneously, within the Moon, α_{inv} varies within a relatively narrow range of values 19–24° (Shkuratov *et al.*, 1992).

Numerous laboratory measurements of light scattering by single particles having various properties show that their average angular profile of degree of linear polarization is qualitatively similar to that found for astronomical targets (Muñoz *et al.*, 2000; 2001; Hovenier *et al.*, 2003). The same is found in measurements of light scattering by powder-like surfaces (e.g., Woessner and Hapke, 1987; Shkuratov and Opanasenko, 1992; Hadamcik *et al.*, 2002; Shkuratov *et al.*, 2006).

The principal parameters characterizing the overall profile of angular dependence of linear polarization degree are the amplitudes of the NPB and PPB, $P_{\min}$ and $P_{\max}$, and their locations, $\alpha_{\min}$ and $\alpha_{\max}$ (e.g., Dollfus and Bowell, 1971; Shkuratov *et al.*, 1992). Note that the inversion angle α_{inv} and slope of the polarization

curve h near the inversion angle are also considered as valuable characteristics of the linear polarization profile (e.g., Zellner and Gradie, 1976; Chernova *et al.*, 1993). Nevertheless, it is obvious that the latter two parameters are not independent; whereas, to a large extent, they are defined through peculiarities of the NPB and PPB. As a consequence, the slope h has no simple connection with dust-particle properties (Zubko *et al.*, 2011).

In the top and middle panels of Figs. 2.13–2.15, we present the principal characteristics of angular dependence of linear polarization $P_{\min}$, $\alpha_{\min}$, $P_{\max}$, and $\alpha_{\max}$ for irregular particles with different morphology and refractive indices m. Note that the minimum of negative polarization was sought only within a small phase angle range $\alpha = 0$–45°. Such a limitation on the range of phase angles is introduced in order to prevent misidentification of the NPB, which can be provoked by very deep negative polarization produced by some particles at intermediate phase angles, as, for instance, in the case of random Gaussian particles with $x = 14$ and $m = 1.6 + 0.0005i$ (see Fig. 2.12). Similarly, we search for the maximum of positive polarization in a range of phase angles $\alpha = 0$–135°, in order to exclude from our consideration the resonant-like spikes in the polarization profile occurring near forward scattering angles, which can be observed, for example, for rough-surface spheres with $x = 10$ and $m = 1.5 + 0.1i$ (see Fig. 2.11). Obviously, such features are not related to the angular dependence of the degree of linear polarization observed for cosmic dust particles and most samples measured under laboratory conditions.

As one can see in Fig. 2.13, irregularly shaped particles with various morphologies have surprisingly similar behavior in the parameters $P_{\min}$, $\alpha_{\min}$, $P_{\max}$, and $\alpha_{\max}$ with size parameter x; whereas, for fixed x, their angular profiles of polarization are completely different (see Figs. 2.10–2.12). For instance, all types of particles do not produce the negative polarization at $x = 2$; whereas, the effect appears within the range of $x = 4$–8 and, then, grows almost monotonically up to largest size parameter that we considered $x = 14$. The profiles for rough-surface spheres and debris of spheres show slightly oscillatory behavior around the average profile. We have already mentioned the resonance behavior of rough-surface spheres, and this could be another manifestation. While the amplitude of negative polarization substantially varies for different types of irregular particles, the locations of the polarization minima reveal good quantitative agreement between some particles types with $x \geq 8$. In general, one can distinguish two groups of particles and one specific case of rough-surface spheres. The first group consists of strongly damaged spheres and debris of spheres. Simultaneously, the second group includes agglomerated debris particles, pocked spheres, and random Gaussian particles. Interestingly, the particles within these groups produce quantitatively similar profiles for $P_{\min}$ even though these particles have completely different structure and values for packing density $\langle\rho\rangle$ (see sub-section 2.2.1).

Fig. 2.14 shows data for irregular particles with $m = 1.6 + 0.0005i$. The size dependence of $P_{\min}$ has more structure than for the previous case of $m = 1.313 + 0i$. The size dependence of $P_{\min}$ has the largest negative polarization around $x = 4$–8; whereas, the negative polarization appears in tighter range within $x = 4$–6. The NPBs for all the morphologies appear at smaller size parameter x with $m = 1.6 + 0.0005i$ than for $m = 1.313 + 0i$. Similar conclusions can be reached for the highly absorbing particles with $m = 1.5 + 0.1i$. As one can see in

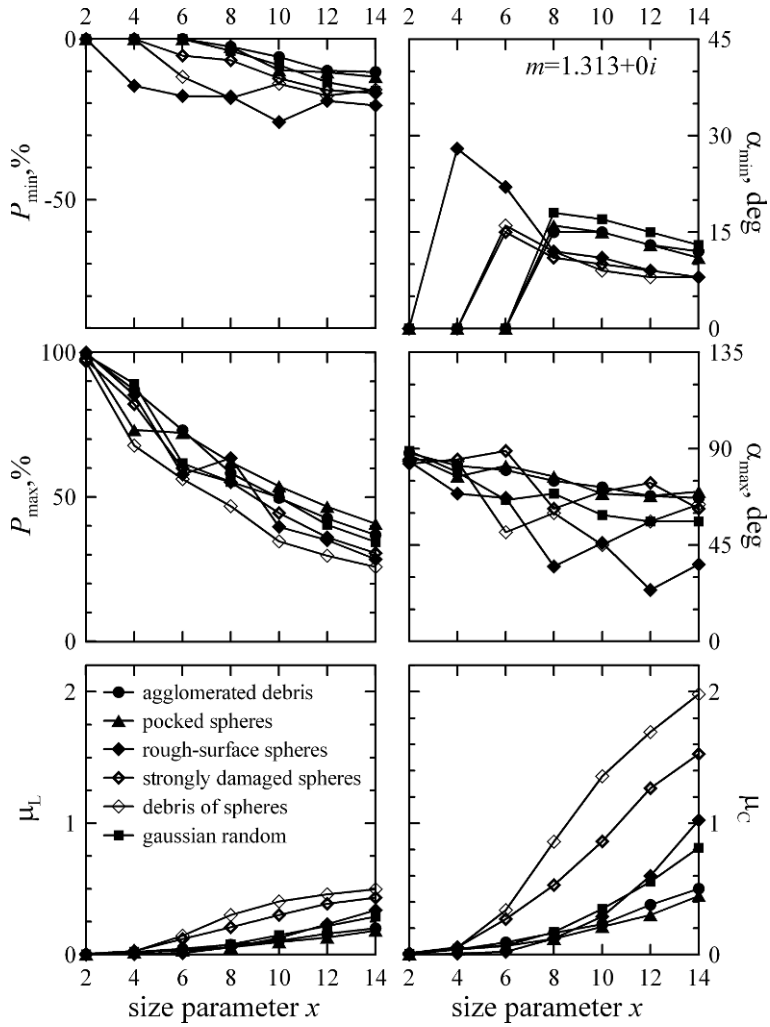

Fig. 2.13. Parameters describing the NPB at small phase angles ($P_{\min}$ and $\alpha_{\min}$) and PPB at intermediate phase angles ($P_{\max}$ and $\alpha_{\max}$), linear and circular polarization ratios μ_{L} and μ_{C} as functions of size parameter x for six types of irregularly shaped particles with $m = 1.313 + 0i$.

Fig. 2.15, except for the case of rough-surface spheres, the NPB of highly absorbing particles appears in the range $x = 6$–8, and the largest values of the negative polarization occurs around $x = 8$–10. Owing to such rapid growth, the spectral dependence of the negative polarization may exhibit a *blue polarimetric color*, i.e., when the decrease in wavelength λ invokes the increase of negative polarization. Indeed, according to the definition of size parameter x, if some irregular particles have $x = 4$ at $\lambda = 0.7\,\mu$m, then the same particles have $x = 8$ at $\lambda = 0.35\,\mu$m. However, as one can see in Figs. 2.13–2.15, the particles with $x = 4$–5 are generally too small in order to produce NPB; whereas, at $x = 8$–10, almost all of them show

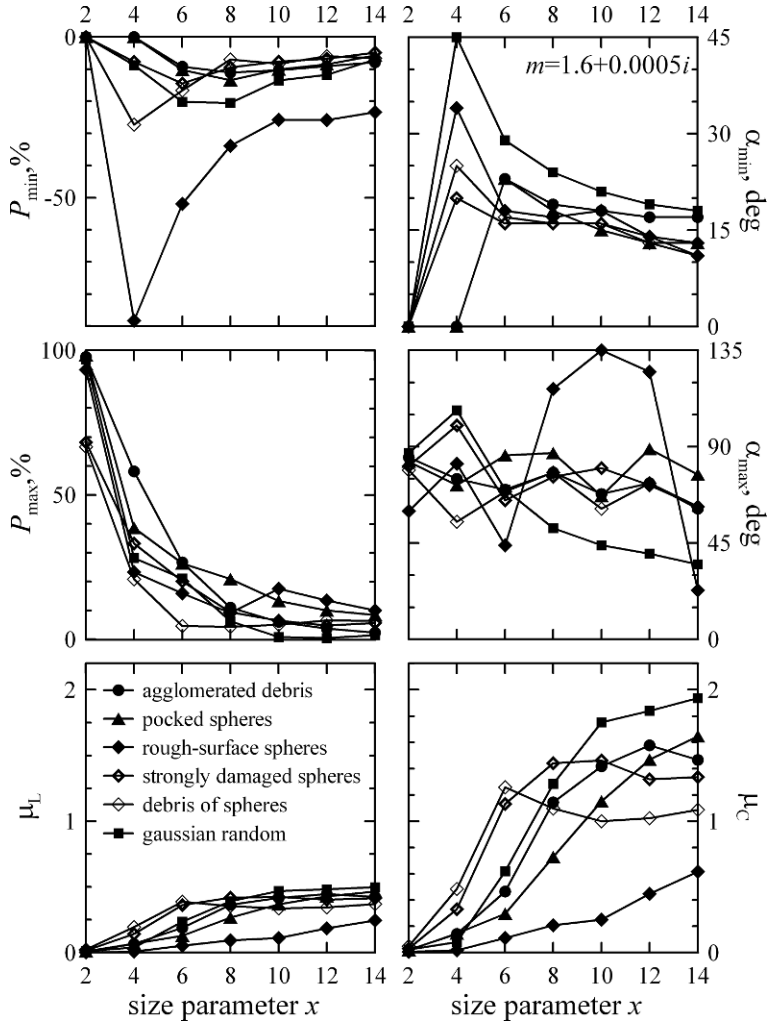

Fig. 2.14. The same as Fig. 2.13 but, for $m = 1.6 + 0.0005i$.

quite noticeable NPBs. As a consequence, the decrease of λ may cause a significant increase of the NPB. This very simple explanation has been successfully used in the quantitative interpretation of blue polarimetric color observed for comet 17P/Holmes during its mega-outburst in October, 2007 (Zubko *et al.*, 2009b).

Again, we consider the distinctive behavior of rough-surface particles with $m = 1.6 + 0.0005i$ and $1.5 + 0.1i$. At $x = 4$, both give rise to an extremely pronounced negative polarization with $|P_{\min}| = 80$–90%. In the case of highly absorbing particles, a similar but less dramatic spike of negative polarization also happens at $x = 8$. Obviously, such a pronounced negative polarization results from the significant sphericity preserved in the shape of the rough-surface particles.

The size dependencies of the phase angle of the polarization minimum $\alpha_{\min}$ for irregular particles with $m = 1.6+0.0005i$ (see Fig. 2.14) are qualitatively consistent

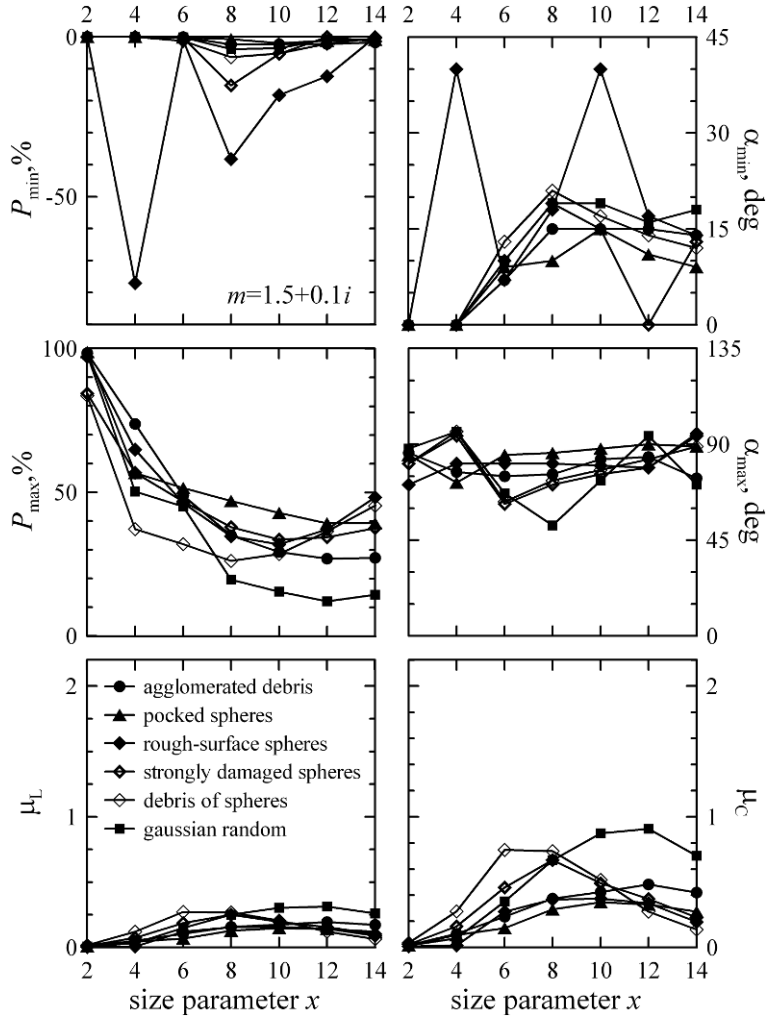

Fig. 2.15. The same as Fig. 2.13 but, for $m = 1.5 + 0.1i$.

with those for $m = 1.313{+}0i$ (compare with Fig. 2.13). That is to say, once the NPB becomes well-developed, the further increase of x decreases $\alpha_{\min}$ monotonically, though nonlinearly. However, particles with larger real part of refractive index produce, in general, higher values of $\alpha_{\min}$. The profiles of $\alpha_{\min}$ as a function of x are different for highly absorbing particles (Fig. 2.15) and weakly absorbing particles. Again, the most irregular behavior corresponds to rough-surface spheres. The other cases have qualitatively similar size-dependences of $\alpha_{\min}$. For instance, in the size range $x < 8$–10, the increase of size parameter x increases the phase angle of polarization minimum $\alpha_{\min}$; whereas, the further increase of size parameter results in a decrease of $\alpha_{\min}$. Note that such a profile of $\alpha_{\min}$ vs. x is qualitatively consistent with what was found for weakly absorbing particles, though, in the case of highly absorbing particles, the growth of $\alpha_{\min}$ to its maximal value is not that

rapid. Finally, for particles with $m = 1.5 + 0.1i$, the profiles $\alpha_{\min}$ vs. x can be distorted by a small surge of positive polarization, appearing near backscattering $\alpha = 0°$ (see Figs. 2.11 and 2.12).

As one can see in Fig. 2.13, while the size parameter x grows, the maximal value of linear polarization $P_{\max}$ almost systematically decreases with only one exception for rough-surface spheres near $x = 8$. Although differences between profiles $P_{\max}$ vs. x for particles with different morphology are quite visible, they are not dramatic. Qualitatively the same conclusions can be made for particles with $m = 1.6 + 0.0005i$ (see Fig. 2.14). However, the particles with higher refractive index have substantially greater nonlinear profiles $P_{\max}$ vs. x. Note also that, for the case of $m = 1.313 + 0i$, $P_{\max}$ decreases about three times through the studied range x; whereas, for $m = 1.6 + 0.0005i$, that decrease is about an order of magnitude. Unlike the cases of weak absorption, irregular particles with $m = 1.5 + 0.1i$ show non-monotonic behavior through the range of $x = 2$–14 (see Fig. 2.15). Except for the case of pocked spheres, all size-dependencies of $P_{\max}$ show a minimum in the $x = 8$–12 range. For instance, in the case of agglomerated debris particles, the minimum occurs at $x = 12$; whereas, growth of $P_{\max}$ between $x = 12$ and 14 is only slight. Therefore, one can suppose that the case of pocked spheres is not really exceptional; instead, the profile $P_{\max}$ vs. x a has minimum at $x > 14$ and is beyond our calculated range.

Among four parameters describing the angular profile of linear polarization presented in Figs. 2.13–2.15, phase angle of the maximum of positive polarization $\alpha_{\max}$ has the most ambiguous dependence on size parameter x. In the case of optically soft particles (Fig. 2.13), $\alpha_{\max}$ tends to decrease while x increases; whereas, the common profiles are accompanied with significant oscillations. Nevertheless, for particles with $m = 1.6 + 0.0005i$, it is very difficult to identify a systematic behavior (see Fig. 2.14). Note that the significant oscillations are presented also on the generally flat profiles $\alpha_{\max}$ vs. x, corresponding to highly absorbing particles (Fig. 2.15).

2.3.2.3 Linear and circular polarization ratios μ_{L} and μ_{C}, and geometric albedo A

In radar applications, two important parameters quantifying electromagnetic scattering are the *linear* and *circular polarization ratios* μ_{L} and μ_{C} (e.g., Ostro, 1993; Mishchenko and Liu, 2007; Zubko *et al.*, 2008). In the case of a fully polarized incident light, the scattered light can be expressed as consisting of two fully polarized components. One component has the same state of polarization as the incident light and is often referred to as the co-polarized component. The cross-polarized component is orthogonally polarized to the incident wave. In the case of linearly polarized incident light, the linear polarization ratio is defined as the ratio of cross- to co-polarized parts of the scattered light; whereas, for circularly polarized incident light, it is more convenient do define the circular polarization ratio as the ratio of co- to cross-polarized parts of the scattered light (Ostro, 1993). In terms of the Mueller matrix elements the ratios are expressed as follows (e.g., Mishchenko and Liu, 2007):

$$\mu_{\mathrm{L}} = \frac{M_{11} - M_{22}}{M_{11} + 2M_{12} + M_{22}}, \quad \mu_{\mathrm{C}} = \frac{M_{11} + M_{44}}{M_{11} - M_{44}}. \tag{7}$$

Obviously, in the general case, both ratios depend on phase angle α. However, in radar applications, the most frequently used case corresponds to backscattering $\alpha = 0°$. Note that, for such specific geometry of electromagnetic scattering, averaging over an ensemble of sample particles and/or their orientations provides $M_{12} = 0$. Therefore, the definition for μ_L in eq. (7) can be simplified. According to radar measurements of all planetary targets, $\mu_L < 1$ and $\mu_L < \mu_C$ (Ostro, 1993). Moreover, as shown in previous studies of agglomerates of perfect spheres (e.g., Mishchenko and Liu, 2007; Mishchenko *et al.*, 2009) and irregularly shaped compact and fluffy particles (Zubko et al., 2008), the same relations hold true for targets comparable with wavelength. It is interesting that at exact backscattering, the ensemble of independent randomly oriented dipoles result in $\mu_L = 1/3$ and $\mu_C = 1$ (Long, 1965; Ostro, 1993).

In the bottom panels of Figs. 2.13–2.15, we show data for the linear (left) and circular (right) polarization ratios of irregular particles with different morphology. The relationships $\mu_L < 1$ and $\mu_L < \mu_C$ found for planetary targets, agglomerates of spherical and non-spherical grains, and independently scattering dipoles remain valid for all morphologies, refractive indices m, and size parameters x, presented in the current review. For instance, the ratio of linear polarization μ_L remains less than 0.5. In the case of optically soft particles (see Fig. 2.13) μ_L grows almost monotonically with x. To a large extent, such behavior can be found for $m = 1.6 + 0.0005i$ (Fig. 2.14). However, in the latter case, there are some exceptions; the most visible of them being for the debris of spheres. In the case of highly absorbing particles (Fig. 2.15), the size-dependencies of μ_L for all particle morphologies are not monotonic, having a maximum in the range $x = 6$–12. Note that in the case of high material absorption, the amplitude of curves μ_L vs. x is systematically less than in the case of weak material absorption.

As mentioned previously, the circular polarization ratio μ_C systematically exceeds the linear polarization ratio μ_L; however, it remains less than 2 for the case of weak absorption, and 1 for highly absorbing particles. The profiles μ_C vs. x are consistent with those for μ_L. In particular, from Figs. 2.13–2.15, one could conclude that for a given morphology of irregular particles and refractive index m, curves for μ_C and μ_L are different only by a scaling factor.

Another parameter of light scattering by single particles defined at $\alpha = 0°$ is the *geometric albedo* A. This parameter describes the ratio of the intensity backscattered by the particle to that scattered by a white disk of the same geometric cross-section G in accordance with Lambert's law (e.g., Hanner *et al.*, 1981; Hanner, 2003):

$$A = \frac{M_{11}(0°)\pi}{k^2 G}. \tag{8}$$

Here, $M_{11}(0°)$ is the corresponding element of the Mueller matrix at $\alpha = 0°$ and k is the wavenumber. In other words, the geometric albedo A equates to the backscattering efficiency of target particles.

As one can see in Fig. 2.16, the geometric albedo A is substantially varied through the range of size parameter $x = 2$–14. In general, the profile A vs. x has one of two distinctive features. The geometric albedo A may continuously grow with size parameter x, as in the case of optically soft particles and random Gaussian particles and both types of fluffy particles with $m = 1.6 + 0.0005i$. Alternatively, the size-

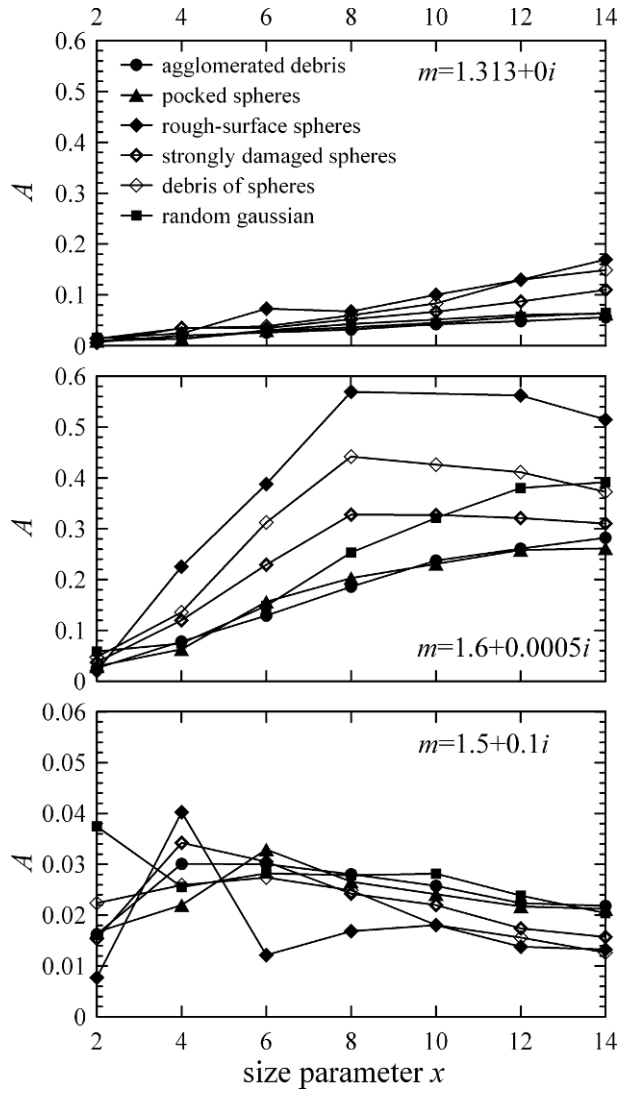

Fig. 2.16. Geometric albedo A as a function of size parameter x for six types of irregularly shaped particles. The top panels show the case of $m = 1.313 + 0i$, the middle panels show the case of $m = 1.6 + 0.0005i$, and the bottom panels show the case of $m = 1.5 + 0.1i$.

dependence of A may be non-monotonic, having a maximum in the range $x = 2$–8. Note that all the highly absorbing particles reveal a maximum in their geometric albedo A in the $x = 2$–4 range; whereas, rough-surface spheres, strongly damaged spheres, and debris of spheres produce maximum A at larger size parameters $x \sim 8$.

We note that the differences in the overall amplitude of albedo for particles with different refractive indices m are especially great. For instance, the highest geometric albedo A (up to 0.6) is produced by irregular particles with $m = 1.6 + 0.0005i$. Simultaneously, optically soft particles present a moderate am-

plitude in curves A vs. x (up to 0.18); whereas, the lowest albedo (up to only 0.04) can be found for highly absorbing particles. Interestingly, the lowest geometric albedo for particles with $m = 1.6 + 0.0005i$ observed at $x = 2$, is nearly coincident with the highest albedo for particles with $m = 1.5 + 0.1i$. Note, the geometric albedo of cometary dust particles averaged over the entire coma is estimated as $A = 0.05$ (Hanner, 2003). As one can see in Fig. 2.16, such a low geometric albedo can be obtained with either very small ($x \leq 2$) or highly absorbing particles. However, the average coma produces a NPB at small phase angles (e.g., Kiselev and Chernova, 1981; Chernova *et al.*, 1993; Hadamcik and Levasseur-Regourd, 2003), which is inconsistent with small particles (see Figs. 2.13–2.15 for size-dependences of $P_{\min}$). Therefore, low geometric albedo A of cometary dust particles suggests high absorption material.

2.4 Conclusion

In the present review, we have presented and discussed numerous aspects of light scattering by irregularly shaped particles having different morphologies and sizes comparable with the wavelength of incident radiation. Almost all characteristics of light scattering substantially depend on the morphology, constituent material, and size of particles. One principle goal is to make some principal characterization of the target particles (such as, the packing density, degree of absorption, real part of refractive index and size parameter x) from their light scattering. Of course, some *a priori* information on target particles will significantly simplify the remote-sensing inversion.

In general, the differential light-scattering parameters are more sensitive to the physical properties of particles than are the integral parameters. One of the most informative characteristic of light scattering is the angular dependence of the degree of linear polarization. In particular, the presence of the NPB at small phase angles indicates the particles are comparable with wavelength. Moreover, the shape of NPB and location of the polarization minimum $\alpha_{\min}$ strongly and, more or less predictably, depend on the size parameter of the particles; whereas, a simultaneous analysis of characteristics of NPB and positive polarization branch (PPB) at intermediate phase angles can be used to retrieve material absorption.

Acknowledgments

I thank Prof. Yuriy Shkuratov (Kharkov National University, Ukraine), Dr Gorden Videen (Army Research Laboratory, USA), and Prof. Karri Muinonen (University of Helsinki, Finland) for their permanent support of my research and, in particular, for the valuable comments on this review. This work is partially supported by the Academy of Finland (contract 1127461). This work was partially supported by NASA program for Outer Planets Research (grant NNX10AP93G).

References

Artymowicz, P., 1988: Radiation pressure forces on particles in the Beta Pictoris system, *Astrophys. J.*, **335**, L79–L82.

Augereau, J.-C., Beust, H., 2006: On the AU Microscopii debris disk. Density profiles, grain properties, and dust dynamics, *Astron. Astrophys.*, **455**, 987–999.

Bauer, S. E., Mishchenko, M. I., Lacis, A. A., Zhang, S., Perlwitz, J., Metzger, S. M., 2007: Do sulfate and nitrate coatings on mineral dust have important effects on radiative properties and climate modeling?, *J. Geophys. Res.*, **112**, D06307.

Belskaya, I. N., Shkuratov, Yu. G., Efimov, Yu. S., Shakhovskoy, N. M., Gil-Hutton, R., Cellino, A., Zubko, E. S., Ovcharenko, A. A., Bondarenko, S. Yu., Shevchenko, V. G., Fornasier, S., Barbieri, C., 2005: The F-type asteroids with small inversion angles of polarization, *Icarus*, **178**, 213–221.

Boehnhardt, H., Tozzi, G.P., Bagnulo, S., Muinonen, K., Nathues A., Kolokolova, L., 2008: Photometry and polarimetry of the nucleus of comet 2P/Encke, *Astron. Astrophys.*, **489**, 1337–1343.

Bohren, C.F., Huffman, D.R., 1983: *Absorption and Scattering of Light by Small Particles*, New York: John Wiley.

Bowell, E., Hapke, B., Domingue, D., Lumme, K., Peltoniemi, J., Harris, A. W., 1989: Application of photometric models to asteroids, in *Asteroids II*, R. Binzel *et al.* (eds), University of Arizona Press, Tucson, 524–556.

Brownlee, D. E., Joswiak, D. J., Schlutter, D. J., Pepin, R. O., Bradley, J. P., Love, S. G., 1995: Identification of individual cometary IDP's by thermally stepped He release, *Lunar Planet. Sci. Conf. XXVI*, 183–184.

Brownlee, D., Tsou, P., Aléon, J., and 180 coauthors, 2006: Comet 81P/Wild 2 Under a Microscope, *Science*, **314**, 1711–1716.

Burnett, D. S., 2006: NASA returns rocks from a comet, *Science*, **314**, 1709–1710.

Burns, J. A., Lamy, P. L., Soter, S., 1979: Radiation forces on small particles in the solar system, *Icarus*, **40**, 1–48.

Busemann, H., Nguyen, A. N., Cody, G. D., Hoppe, P., Kilcoyne, A. L. D., Stroud, R. M., Zega, T. J., Nittler, L. R., 2009: Ultra-primitive interplanetary dust particles from the comet 26P/Grigg-Skjellerup dust stream collection, *Earth and Planetary Science Letters*, **288**, 44–57.

Cellino, A., Belskaya, I. N., Bendjoya, Ph., Di Martino, M., Gil-Hutton, R., Muinonen, K., Tedesco, E. F., 2006: The strange polarimetric behavior of Asteroid (234) Barbara, *Icarus*, **180**, 565–567.

Dai, Z. R., Bradley, J. P., 2001: Iron-nickel sulfides in anhydrous interplanetary dust particles, *Geochimica et Cosmochimica Acta*, **65**, 3601–3612.

Dollfus, A., Bowell, E., 1971: Polarimetric Properties of the Lunar Surface and its Interpretation. Part I. Telescopic Observations, *Astron. Astrophys.*, **10**, 29–53.

Draine, B., 1988: The discrete-dipole approximation and its application to the interstellar graphite grains, *Astrophys. J.*, **333**, 848–872.

Draine, B. T., Flatau, P. J., 1994: The discrete dipole approximation for scattering calculations, *J. Opt. Soc. Am. A*, **11**, 1491–1499.

Dumont, R., Sanchez, F., 1975: Zodiacal light photopolarimetry. II. Gradients along the ecliptic and the phase functions of interplanetary matter, *Astron. Astrophys.*, **38**, 405–412.

Fulle, M., 2004: Motion of cometary dust, in *Comets II*, M. C. Festou *et al.* (eds), University of Arizona Press, Tucson, 565–575.

Chernova, G. P., Kiselev, N. N., Jockers, K., 1993: Polarimetric characteristics of dust particles as observed in 13 comets – Comparisons with asteroids, *Icarus*, **103**, 144–158.

Goodman, J. J., Draine, B. T., Flatau, P. J., 1991: Application of fast-Fourier-transform techniques to the discrete-dipole approximation, *Opt. Lett*, **16**, 1198–1200.

Hadamcik, E., Levasseur-Regourd, A.C., 2003: Imaging polarimetry of cometary dust: different comets and phase angles, *J. Quant. Spectrosc. Radiat. Transfer*, **79–80**, 661–678.

Hadamcik, E., Renard, J. B., Worms, J. C., Levasseur-Regourd, A. C., Masson, M., 2002: Polarization of light scattered by fluffy particles (PROGRA^2 experiment), *Icarus*, **155**, 497–508.

Hanner, M. S., 2003: The scattering properties of cometary dust, *J. Quant. Spectrosc. Radiat. Transfer*, **79–80**, 695–705.

Hanner, M. S., Bradley, J. P., 2004: Composition and mineralogy of cometary dust, in *Comets II*, M. C. Festou *et al.* (eds), University of Arizona Press, Tucson, 555–564.

Hanner, M. S., Giese, R. H., Weiss, K., Zerull, R., 1981: On the definition of albedo and application to irregular particles, *Astron. Astrophys.*, **104**, 42–46.

Hovenier, J. W., Volten, H., Muñoz, O., van der Zande, W. J., Waters, L. B. F. M., 2003: Laboratory studies of scattering matrices for randomly oriented particles: potentials, problems, and perspectives, *J. Quant. Spectrosc. Radiat. Transfer*, **79–80**, 741–755.

van de Hulst, H.C., 1981: *Light scattering by small particles*, New York: Dover.

Jessberger, E. K., Stephan, T., Rost, D., Arndt, P., Maetz, M., Stadermann, F. J., Brownlee, D. E., Bradley, J. P., Kurat, G., 2001: Properties of Interplanetary Dust: Information from Collected Samples, in *Interplanetary Dust*, E. Grün *et al.* (eds), Springer-Verlag, Berlin, 253–294.

Kimura, H., Mann, I., 1998: Radiation pressure cross-section for fluffy aggregates, *J. Quant. Spectrosc. Radiat. Transfer*, **60**, 425–438.

Kimura, H., Mann, I., 2004: Light scattering by large clusters of dipoles as an analog for cometary dust aggregates, *J. Quant. Spectrosc. Radiat. Transfer*, **89**, 155–164.

Kimura, H., Okamoto, H., Mukai, T., 2002: Radiation pressure and the Poynting-Robertson effect for fluffy dust particles, *Icarus*, **157**, 349–361.

Kiselev, N. N., Chernova, G. P., 1981: Phase functions of polarization and brightness and the nature of cometary atmosphere particles, *Icarus*, **48**, 473–481.

Kokhanovsky, A. A., 2008: *Aerosol Optics: Light absorption and scattering by particles in the atmosphere*, New York: Springer–Praxis.

Levasseur-Regourd, A. C., Dumont, R., Renard, J. B., 1990: A comparison between polarimetric properties of cometary dust and interplanetary dust particles, *Icarus*, **86**, 264–272.

Lindqvist, H., Muinonen, K., Nousiainen, T., 2009: Light scattering by coated Gaussian and aggregate particles, *J. Quant. Spectrosc. Radiat. Transfer*, **110**, 1398–1410.

Long, M., 1965: On the polarization and the wavelength dependence of sea echo, *IEEE Transactions on Antennas and Propagation*, **13**, 749–754.

Lumme, K., Rahola, J., Hovenier J. W., 1997: Light scattering by dense clusters of spheres, *Icarus*, **126**, 455–469.

Macke, A., Mishchenko, M. I., 1996: Asymmetry parameters of the phase function for large particles with multiple internal inclusions, *Bull. Am. Astron. Soc.*, **28**, 1122.

Mazets, E. P., Aptekar, R. L., Golenetskii, S. V., Guryan, Yu. A., Dyachkov, A. V., Ilyinskii, V. N., Panov, V. N., Petrov, G. G., Savvin, A. V., Sagdeev, R. Z., Sokolov, I. A., Khavenson, N. G., Shapiro, V. D., Shevchenko, V. I., 1986: Comet Halley dust environment from SP-2 detector measurements, *Nature*, **321**, 276–278.

Mishchenko, M. I., 1994: Asymmetry parameters of the phase function for densely packed scattering grains, *J. Quant. Spectrosc. Radiat. Transfer*, **52**, 95–110.

Mishchenko, M. I., Liu, L., 2007: Weak localization of electromagnetic waves by densely packed many-particle groups: Exact 3D results, *J. Quant. Spectrosc. Radiat. Transfer*, **106**, 616–621.

Mishchenko, M. I., Dlugach, J. M., Liu, L., Rosenbush, V. K., Kiselev, N. N., Shkuratov, Yu. G., 2009: Direct solutions of the Maxwell equations explain opposition phenomena observed for high-albedo Solar system objects, *Astrophys. J.*, **705**, L118–L122.

Muinonen, K., Nousiainen, T., Fast, P., Lumme, K., Peltoniemi, J.I., 1996: Light scattering by Gaussian random particles: ray optics approximation, *J. Quant. Spectrosc. Radiat. Transfer*, **55**, 577–601.

Muinonen, K., Zubko, E., Tyynelä, J., Shkuratov, Yu. G., Videen G., 2007: Light scattering by Gaussian random particles with discrete-dipole approximation, *J. Quant. Spectrosc. Radiat. Transfer*, **106**, 360–377.

Muñoz, O., Volten, H., de Haan, J. F., Vassen, W., Hovenier, J. W., 2000: Experimental determination of scattering matrices of olivine and Allende meteorite particles, *Astron. Astrophys.*, **360**, 777–788.

Muñoz, O., Volten, H., de Haan, J. F., Vassen, W., Hovenier, J. W., 2001: Experimental determination of scattering matrices of randomly oriented fly ash and clay particles at 442 and 633 nm, *J. Geophys. Res.*, **106**, 22833–22844.

Muñoz, O., Volten, H., Hovenier, J. W., Min, M., Shkuratov, Yu. G., Jalava, J. P., van der Zande, W. J., Waters, L. B. F. M., 2006: Experimental and computational study of light scattering by irregular particles with extreme refractive indices: hematite and rutile. *Astron. Astrophys.*, **446**, 525–535.

Nousiainen, T., 2009: Optical modeling of mineral dust particles: A review, *J. Quant. Spectrosc. Radiat. Transfer*, **110**, 1261–1279.

Nousiainen, T., Muinonen, K., 2007: Surface-roughness effects on single-scattering properties of wavelength-scale particles, *J. Quant. Spectrosc. Radiat. Transfer*, **106**, 389–397.

Ostro, S. J., 1993: Planetary radar astronomy, *Rev. Mod. Phys.*, **65**, 1235–1279.

Penttilä, A., Zubko, E., Lumme, K., Muinonen, K., Yurkin, M. A., Draine, B., Rahola, J., Hoekstra, A. G., Shkuratov, Yu., 2007: Comparison between discrete dipole implementations and exact techniques, *J. Quant. Spectrosc. Radiat. Transfer*, **106**, 417–436.

Rosenbush, V., Kolokolova, L., Lazarian, A., Shakhovskoy, N., Kiselev N., 2007: Circular polarization in comets: Observations of Comet C/1999 S4 (LINEAR) and tentative interpretation, *Icarus*, **186**, 317–330.

Shen, Y., Draine, B. T., Johnson, E. T., 2009: Modeling porous dust grains with ballistic aggregates. II. Light scattering properties, *Astrophys. J.*, **696**, 2126–2137.

Shkuratov, Yu.G., Opanasenko, N.V., 1992: Polarimetric and photometric properties of the Moon: Telescope observation and laboratory simulation. 2. The positive polarization, *Icarus*, **99**, 468–484.

Shkuratov, Yu.G., Opanasenko, N.V., Kreslavsky, M.A., 1992: Polarimetric and photometric properties of the Moon: Telescope observation and laboratory simulation. 1. The negative polarization, *Icarus*, **95**, 283–299.

Shkuratov, Yu., Bondarenko, S., Ovcharenko, A., Pieters, C., Hiroi, T., Volten, H., Munos, O., Videen, G., 2006: Comparative studies of the reflectance and degree of linear polarization of particulate surfaces and independently scattering particles, *J. Quant. Spectrosc. Radiat. Transfer*, **100**, 340–358.

Tyynelä, J., Zubko, E., Muinonen, K., Videen G., 2010: Interpretation of single-particle negative polarization at intermediate scattering angles, *Appl. Opt.*, submitted.

Videen, G., 2002: Polarization opposition effect and second-order ray tracing, *Appl. Opt.*, **41**, 5115–5121.

Vilaplana, R., Moreno, F., Molina, A., 2006: Study of the sensitivity of size-averaged scattering matrix elements of nonspherical particles to changes in shape, porosity and refractive index, *J. Quant. Spectrosc. Radiat. Transfer*, **100**, 415–428.

Volten, H., Muñoz, O., Hovenier, J. W., Rietmeijer, F. J. M., Nuth, J. A., Waters, L. B. F. M., van der Zande, W. J., 2007: Experimental light scattering by fluffy aggregates of magnesiosilica, ferrosilica, and alumina cosmic dust analogs, *Astron. Astrophys.*, **470**, 377–386.

Wickramasinghe, N. C., Wickramasinghe, J. T., 2003: Radiation pressure on bacterial clumps in the solar vicinity and their survival between interstellar transits, *Astrophysics and Space Science*, **286**, 453–459.

Woessner, P., Hapke, B., 1987: Polarization of light scattered by clover, *Remote Sensing of Environ*, **21**, 243–261.

Yurkin, M.A., Hoekstra, A.G., 2007L The discrete dipole approximation: An overview and recent developments, *J. Quant. Spectrosc. Radiat. Transfer*, **106**, 558–589.

Zellner, B., Gradie, J., 1976: Minor planets and related objects. XX - Polarimetric evidence for the albedos and compositions of 94 asteroids, *Astron. J.*, **81**, 262–280.

Zubko, E., Shkuratov, Yu., Muinonen, K., 2001: Light scattering by composite particles comparable with wavelength and their approximation by systems of spheres, *Optics and Spectroscopy*, **91**, 273–277.

Zubko, E. S., Shkuratov, Yu. G., Hart, M., Eversole, J., Videen, G., 2003: Backscattering and negative polarization of agglomerate particles, *Opt. Lett.*, **28**, 1504–1506.

Zubko, E. S., Shkuratov, Yu. G., Hart, M., Eversole, J., Videen, G., 2004: Backscatter of agglomerate particles, *J. Quant. Spectrosc. Radiat. Transfer.*, **28**, 163–171.

Zubko, E., Shkuratov, Yu., Kiselev, N., Videen, G., 2006: DDA simulations of light scattering by small irregular particles with various structure, *J. Quant. Spectrosc. Radiat. Transfer*, **101**, 416–434.

Zubko, E., Muinonen, K., Shkuratov, Yu., Videen, G., Nousiainen, T., 2007: Scattering of light by roughened Gaussian random particles, *J. Quant. Spectrosc. Radiat. Transfer*, **106**, 604–615.

Zubko, E., Kimura, H., Shkuratov, Yu., Muinonen, K., Yamamoto, T., Okamoto, H., Videen, G., 2009a: Effect of absorption on light scattering by agglomerated debris particles, *J. Quant. Spectrosc. Radiat. Transfer*, **110**, 1741–1749.

Zubko, E., Furusho, R., Yamamoto, T., Videen, G., Muinonen, K., 2009b: Interpretation of photo-polarimetric observations of comet 17P/Holmes during outburst in 2007, *Bull. Am. Astron. Soc.*, **41**, 1035.

Zubko, E., Petrov, D., Grynko, Y., Shkuratov, Yu., Okamoto, H., Muinonen, K., Nousiainen, T., Kimura, H., Yamamoto, T., Videen, G., 2010: Validity criteria of the discrete dipole approximation, *Appl. Opt.*, **49**, 1267–1279.

Zubko, E., Videen, G., Shkuratov, Yu., Muinonen, Yamamoto, T., 2011: The Umov effect for single irregularly shaped particles with sizes comparable with wavelength, *Icarus*, **212**, 403–415.

http://www.springer.com/978-3-642-15530-7

Light Scattering Reviews, Vol. 6
Light Scattering and Remote Sensing of Atmosphere and Surface
Kokhanovsky, A. (Ed.)
2012, XXII, 336 p., Hardcover
ISBN: 978-3-642-15530-7